

HIGHLY FLUORESCENT CESIUM LEAD TRIBROMIDE NANOCRYSTALS FOR
LUMINESCENCE UP-CONVERSION

A Dissertation

by

BENJAMIN ROMAN

Submitted to the Office of Graduate and Professional Studies of
Texas A&M University
in partial fulfillment of the requirements for the degree of

DOCTOR OF PHILOSOPHY

Chair of Committee,	Matthew T. Sheldon
Committee Members,	Sarbajit Banerjee
	Xiaofeng Qian
	Dong Hee Son
Head of Department,	Simon North

December 2020

Major Subject: Chemistry

Copyright 2020 Benjamin J. Roman

ABSTRACT

Cesium lead tribromide nanocrystals have remarkably high photoluminescence quantum yield due, in part, to their tolerance to the formation of defect states. Further, the most commonly formed defect—excess lead on the nanocrystal surface—can be removed via a facile treatment, increasing their photoluminescence quantum yield to approximately unity. Their efficient fluorescence makes cesium lead tribromide nanocrystals a promising target for luminescence up-conversion, a phenomenon whereby photons with lower energy are converted into emitted photons with higher energy. This optical process has applications in bioimaging, as well as optical energy conversion where up-conversion can be utilized to decrease band-gap and thermalization losses. Here, I discuss the development and study of cesium lead tribromide nanocrystals for luminescence up-conversion.

One method for luminescence up-conversion is so-called hot-electron up-conversion. This mechanism utilizes the hot electrons generated in a metal to drive photoluminescence in a semiconductor, a process that is impeded by the quenching of the semiconductor photoluminescence that is typically observed in metal-semiconductor heterostructures. I demonstrate a method for depositing gold nanocrystals onto the surface of CsPbBr_3 nanocrystals, as well as discuss the competing reaction pathway that leads to gold cation exchange with lead in the nanocrystal lattice. I demonstrate that CsPbBr_3 maintains high efficiency photoluminescence with gold nanoparticles deposited on its surface.

Another up-conversion mechanism to which CsPbBr₃ can be applied is one photon up-conversion, also known as anti-Stokes photoluminescence (ASPL). This up-conversion mechanism uses thermal energy from the material to drive up-conversion. If this occurs with efficiency near unity, ASPL depopulates the material's phonon modes leading to a net decrease in temperature. I demonstrate that efficient CsPbBr₃ ASPL does not rely on mid-gap electronic states to act as intermediates. CsPbBr₃ ASPL is shown to cool the local environment of the nanocrystals by as much as 25 °C, using the Raman scattering of a silicon substrate as a reporter for the temperature. Additionally, the thermal scavenging potential of CsPbBr₃ ASPL is shown to be enhanced through coupling to a plasmonic substrate, with a greatly enhanced ASPL photon yield as well as more thermal energy removed from the system per up-converted photon.

For Sarah.

ACKNOWLEDGEMENTS

First and foremost, I would like to thank my committee chair and mentor, Dr. Matthew Sheldon. Your excitement and enthusiasm for science has made my time in your group an amazing experience. Learning from you and working with you has been such a privilege.

I would like to thank my committee members, Dr. Sarbajit Banerjee, Dr. Xiaofeng Qian, and Dr. Dong Hee Son, for their guidance and support throughout the course of this research.

I would also like to thank Dr. Paul Marshall, my undergraduate research advisor at the University of North Texas. I wouldn't be here if it weren't for you. Your classes taught me to love chemistry, and your research made me think that maybe grad school was for me.

I would like to thank the members of the Sheldon group, both past and present, who were sources of great conversation and inspiration. I've enjoyed working with and getting to know every single one of you. Specifically, I want to thank the members of the "synthesis group" whose research I've had the privilege of watching grow and advance from week to week: Je-Ruei Wen, Freddy Rodriguez, Noel Mireles, and Kylie Lytle. You've made my time at Texas A&M such a joy. Even when the stresses of research felt overwhelming, I knew that I could count on you all for a good conversation, some scientific advice, or a sympathetic ear.

Maelani Negrito, Dr. Shengxiang Wu, Hsu-Cheng Cheng, and Dr. Nicki Hogan, I am glad to have started this journey with you all. Our time together in the Sheldon Group has been singularly unique. A lab can only have one first-cohort of graduate students. I am proud to have been a part of that with you. I couldn't have asked for a better group of scientists with which to take these first steps.

I would like to thank the many undergraduates who worked with me over the years: Jennifer Miller, Christopher Galick, Joseph Otto, Rachel Downing, Richard Reyes, David Dacres, and Nick Porcellino. Working with you all was one of the most rewarding experiences I had during my time at Texas A&M. Your interest and enthusiasm helped invigorate my love of science, and your questions made me a better researcher. This dissertation would not have been possible without every single one of you.

I would also like to thank Dr. Gisela Lin for her patience and advice. I don't think that these last 8 months would have been possible without your guidance and help.

Thanks to my loving family for their support and encouragement through my academic pursuits. Sara and Isaac, your astounding creativity, talent, and intelligence will always be an inspiration to me. Mom and Dad, I obviously wouldn't be here if it wasn't for you both. It is thanks to you that I am the man that I am today. You encouraged me to ask questions, and you always took the time to answer. You taught me to think through problems carefully, and to have the confidence to try out different solutions. You taught me that if I didn't know something, I could always look it up. If that isn't scientific research, then I don't know what is.

I would especially like to thank William Matthews and Nicki Hogan, who helped keep me sane. Will, you will always be my brother. Thank you for your friendship these last 12 years. Nicki, I can't overstate the impact that you made on my time a grad school. From our regular board game nights to the hours spent arguing over homework—we both had the same answers but disagreed on the reason those answers were correct—your friendship has really kept me going through these last 5½ years.

Sarah Roman, what an adventure this has been. 9½ years together, 3 graduations, 5½ years of grad school, 5 years of marriage. Thank you for sticking with me through all of it. You've heard it all and seen it all. You've known both the highs and the lows of this process and have supported me through all of them.

Finally, I would like to thank my cats, Freya and Ceridwen, who kept my lap warm while writing this dissertation and reminded me when it was time to take a break and feed them.

CONTRIBUTORS AND FUNDING SOURCES

Contributors

This work was supervised by a dissertation committee consisting of Professor Matthew Sheldon (advisor), Professor Sarbajit Banerjee, Professor Dong Hee Son, and Professor Xiaofeng Qian of the Department of Materials Science and Engineering.

Christopher Galik and Joseph Otto assisted with developing the gold deposition and cation exchange reactions in Chapter 2. Rachel Downing assisted with the x-ray diffraction measurements in Chapter 2. Noel Mireles Villegas measured the photoluminescence quantum yield for the sample in Chapter 4. Kylie Lytle analyzed the temperature dependence of the photoluminescence in Chapter 4. Dr. Nicki Hogan ran the finite difference time domain calculations for Chapter 5.

All other work conducted for the dissertation was completed by Benjamin Roman independently.

Funding Sources

Graduate study was supported by a fellowship from Texas A&M University and the Association of Former Students.

This work was also made possible in part by the Welch Foundation under Grant Number A-1886, the National Science Foundation under Grant Number CHE-1359175, the Air Force Office of Scientific Research under award number FA9550-16-1-0154, and the Gordon and Betty Moore Foundation through Grant GBMF6882.

NOMENCLATURE

ASPL	anti-Stokes photoluminescence
EDS	energy dispersive X-ray spectroscopy
EQE	external quantum efficiency
FWHM	full-width at half-maximum
HRTEM	high resolution transmission electron microscopy
IQE	internal quantum efficiency
OA	oleic acid
OAm	oleylamine
ODE	1-octadecene
PL	photoluminescence
PLQY	photoluminescence quantum yield
QY	quantum yield
SSPL	Stokes shifted photoluminescence
TEM	transmission electron microscopy
XRD	X-ray diffraction

TABLE OF CONTENTS

	Page
ABSTRACT.....	ii
DEDICATION.....	iv
ACKNOWLEDGEMENTS.....	v
CONTRIBUTORS AND FUNDING SOURCES.....	viii
NOMENCLATURE.....	ix
TABLE OF CONTENTS.....	x
LIST OF FIGURES.....	xii
LIST OF TABLES.....	xv
1. INTRODUCTION.....	1
1.1. Cesium Lead Trihalide Nanocrystals.....	1
1.2. Multi-photon Luminescence Up-conversion.....	2
1.3. One Photon Luminescence Up-conversion.....	5
2. GOLD DEPOSITION ON CESIUM LEAD TRIBROMIDE NANOCRYSTALS	10
2.1. Introduction.....	10
2.2. Methods.....	12
2.2.1. Synthesis of CsPbBr ₃ Nanoparticles.....	12
2.2.2. Gold deposition and cation exchange reactions.....	13
2.2.3. Characterization Methods.....	15
2.3. Results and Discussion.....	17
2.4. Conclusions.....	25
3. THE ROLE OF MID-GAP STATES IN ONE PHOTON UP-CONVERSION.....	27
3.1. Introduction.....	27
3.2. Methods.....	31
3.2.1. Synthesis of CsPbBr ₃ Nanoparticles.....	31
3.2.2. Characterization Methods.....	32
3.3. Results and Discussion.....	33

3.4. Conclusions.....	38
4. OPTICALLY DRIVEN COOLING VIA ONE PHOTON UP-CONVERSION	40
4.1. Introduction.....	40
4.2. Methods	43
4.2.1. Synthesis of CsPbBr ₃ Nanoparticles	43
4.2.2. Characterization Methods	44
4.3. Results and Discussion	45
4.4. Conclusions.....	57
5. PLASMONIC ENHANCEMENT OF ONE PHOTON UP-CONVERSION	59
5.1. Introduction.....	59
5.2. Methods	61
5.2.1. Preparation of Samples	61
5.2.2. Characterization Methods	62
5.3. Results and Discussion	63
5.4. Conclusions.....	71
6. CONCLUSIONS.....	73
REFERENCES	76

LIST OF FIGURES

	Page
<p>Figure 2.1: (a) Picture of CsPbBr₃ (left), Cs₂Au₂Br₆ (middle) and Au-CsPbBr₃ (right) in white light (top) and UV excitation (bottom). (b) TEM of CsPbBr₃. (c) TEM of CsPbBr₃ after gold cation exchange. (d) TEM of CsPbBr₃ with gold deposition. (e) TEM of Au-CsPbBr₃ heterostructures showing lattice spacings corresponding to the (202) plane of orthorhombic CsPbBr₃ (5.8 Å) and the (100) plane of cubic Au (3.7 Å). (f) Powder x-ray diffraction (XRD) diffractogram of CsPbBr₃ (blue trace), CsPbBr₃ with 3.0 nm deposition (orange trace), and the Cs₂Au₂Br₆ exchange product (yellow trace). A characteristic section of the diffractogram is shown. The visible peaks correspond to the (040) and (202) planes of both orthorhombic CsPbBr₃ and tetragonal Cs₂Au₂Br₆. The asterisk denotes the peak characteristic of the (111) plane of cubic gold.....</p>	16
<p>Figure 2.2: (a) Absorbance of CsPbBr₃ before and after Au metal deposition compared to the cation exchange product, Cs₂Au₂Br₆. (b) Photoluminescence of CsPbBr₃ before and after Au metal deposition, normalized to 510 nm PLQY.</p>	19
<p>Figure 2.3: (a) Spectra showing the normalized absorbance and photoluminescence of Cs₂Au₂Br₆. (b) HRTEM image showing a partially exchange nanocrystal. Resolved lattice spacings correspond with the (202) plane of orthorhombic CsPbBr₃ and the (103) plane of tetragonal Cs₂Au₂Br₆. (c) Normalized XRD diffractograms showing the progression of cation exchange as 0.5 mL AuBr₃ solutions with increasing concentration are added to identical amounts of CsPbBr₃.</p>	21
<p>Figure 2.4: Energy dispersive x-ray spectrum demonstrating the absence of Pb after the cation exchange reaction of AuBr₃ with CsPbBr₃.</p>	23
<p>Figure 3.1: Optical characterization of CsPbBr₃, with (green) and without (red) NH₄SCN treatment. (a) Absorbance and above-gap excitation photoluminescence. (b) Photoluminescence under 460 nm (dashed) and 532 nm (solid) excitation. (c) Normalized log-log plot of the power dependence of CsPbBr₃ photoluminescence under 532 nm excitation.</p>	34
<p>Figure 3.2: Arrhenius plots for CsPbBr₃, with (green) and without (red) NH₄SCN treatment.</p>	36
<p>Figure 3.3: Power dependent spectral shift (blue circles, left axis) and broadening (orange diamonds, right axis) of NH₄SCN-treated CsPbBr₃.</p>	37

Figure 4.1: CsPbBr ₃ absorbance (blue) and anti-Stokes photoluminescence when the nanocrystals are at 25 °C (purple) and 65 °C (green).	42
Figure 4.2: CsPbBr ₃ anti-Stokes photoluminescence spectral changes during below-gap (532 nm) excitation. (a) Excitation fluence dependent decrease in ASPL intensity over time. Blue squares, green diamonds, and red circles correspond to excitation fluences of 300, 1500, and 3000 W/cm ² respectively. (b) CsPbBr ₃ pumped below-gap (532 nm) at a fluence for 15 W/cm ² for 100 seconds. The laser was then blocked, as indicated by the dotted line. The laser was unblocked periodically to check the ASPL intensity. (c) ASPL decrease in full-width at half-max with an excitation fluence of 3000 W/cm ² . (d) Red shift of ASPL spectral position with an excitation fluence of 3000 W/cm ² . In (c) and (d) the dashed line is a linear fit to the data. These data sets are from the same experiment as the red circles in (a).	46
Figure 4.3: NH ₄ SCN treated CsPbBr ₃ excited below gap (532 nm) at a fluence of 4600 W/cm ² until the temperature reached a steady state. The laser fluence was then decreased to 2300 W/cm ² until the temperature once again reached a steady state. The dotted line indicated when the laser fluence was decreased. The temperature was estimated using equation 4.1.	47
Figure 4.4: The temperature reported by the internal thermocouple of a heating stage plotted versus the temperature (right axis) estimated using the change in CsPbBr ₃ ASPL intensity (left axis) according to equation 4.1. The dashed line corresponds to the temperature reported by the thermocouple.	48
Figure 4.5: An Arrhenius plot of the temperature dependence of NH ₄ SCN treated CsPbBr ₃ ASPL over the temperature range 10–24 °C. The estimated energy of activation was 140 meV.	51
Figure 4.6: Monitoring the temperature of CsPbBr ₃ nanocrystals during below-gap excitation (532 nm). The nanoparticles were cooled at an excitation fluence of 300 W/cm ² , followed by a decreased fluence of 30 W/cm ² , the laser being blocked, and then 30 W/cm ² again.	52
Figure 4.7: NH ₄ SCN treated CsPbBr ₃ nanocrystals, pumped below gap (532 nm) at a fluence of 30 W/cm ² . The steady ASPL intensity, and thus the temperature estimated using equation 4.1, indicates that this fluence is too low to overcome heat flux from the nanoparticles' environment. This is the same sample analyzed in Figure 4.6.	53
Figure 4.8: CsPbBr ₃ anti-Stokes photoluminescence spectral changes during below-gap (532 nm) excitation. (a) Excitation fluence dependent decrease in temperature over time. Blue squares, green diamonds, and red circles	

correspond to excitation fluences of 300, 1500, and 3000 W/cm² respectively. This data set is the same as in Figure 4.2a, using equation 4.1 to estimate temperature. Note that the temperatures estimated here are only accurate so long as the ASPL energy of activation holds constant over this temperature range. (b) CsPbBr₃ pumped below-gap (532 nm) at a fluence for 15 W/cm² for 100 seconds. The laser was then blocked. The laser was unblocked periodically to check the ASPL intensity. This is the same data set as in Figure 4.2b, using equation 4.1 to estimate temperature..... 54

Figure 4.9: Silicon Raman scattering resolved simultaneously to CsPbBr₃ ASPL. 55

Figure 4.10: Temperature of CsPbBr₃ nanoparticles during below gap excitation, estimated using the CsPbBr₃ ASPL intensity (green) as well as the anti-Stokes to Stokes Raman scattering ratio of Si (red). At the end of the measurement, the focus was adjusted to maximize the silicon Raman scattering collection efficiency. The final temperature of the silicon substrate is reported as the red x. 56

Figure 5.1: (A) ASPL intensity versus the power law slope of the ASPL excitation power dependence. (B) ASPL Intensity normalized to the SSPL intensity in the same region plotted against the average scavenged thermal energy per photon emitted. The relative ASPL intensity is scaled so that a value of 1 corresponds to the average value for the control..... 67

Figure 5.2: Relative ASPL intensity versus scavenged thermal energy per emitted photon for the sample with uniform Au nanoparticle coverage. The color of each point corresponds to the scavenged thermal energy per photon multiplied by the relative ASPL intensity and normalized to the average corresponding value for the control..... 69

Figure 5.3: Field enhancement of a 40 nm gold nanoparticle surrounded by a material with a refractive index of 2.25..... 71

LIST OF TABLES

	Page
Table 2.1: Perovskite nanocrystal optical properties due to Au metal deposition or Au cation exchange	18
Table 2.2: Au:Pb molar ratio dependence of cation exchange.	25
Table 3.1: Summary of spectral data for above and below-gap excitation.....	30
Table 5.1: Average position, full width at half max, and average thermal energy scavenged by each up-converted photon.....	64

1. INTRODUCTION

1.1. Cesium Lead Trihalide Nanocrystals

Colloidally synthesized cesium lead halide perovskite nanocrystals (CsPbX_3 , $X = \text{Cl, Br, or I}$) were first reported by Protesescu and co-workers in 2015, [1] and since then have been of great interest to the scientific community for their unique optoelectronic and photophysical properties that make them ideally suited for optical applications such as light emitting diodes, [2–4] lasers, [5–7] and solution-processed solar cells. [8–10] CsPbX_3 nanocrystals are cuboid in morphology, typically cubic or orthorhombic with edge lengths of 8–10 nm. They have narrow emission linewidths that can be spectrally tuned across the entire visible spectrum by controlling their compositional stoichiometric ratio of halide ions. This can be accomplished through the ratio of lead halide salts used as precursors during their synthesis, [1] or post-synthetically through anion exchange. [11–13] Remarkably, anion exchange can occur at room temperature if an appropriate halide source is incorporated into the solution of nanocrystals. CsPbX_3 can even act as halide sources for anion exchange—if a solution of CsPbBr_3 is mixed with a solution of CsPbI_3 nanocrystals, the iodide and bromine will exchange until a single population of mixed-halide nanocrystals remains. [11,12,14] This halide exchange is facilitated by the lability of the oleylammonium halide ligands that are bound to the surface of the nanocrystals, as well as the general mobility of the constituent ions through the nanocrystal itself. [15–18]

Perhaps most remarkably, as-synthesized CsPbBr_3 nanocrystals, the material focus of this dissertation, have photoluminescence quantum yield (PLQY) of up to 80%,

even without the passivating layer or surface treatment that is otherwise necessary for high efficiency photoluminescence (PL) in other semiconducting nanocrystals. [1] This is due to their resistance to forming mid-gap defect states that would act as nonradiative loss pathways. CsPbBr₃ nanoparticles are synthesized in a lead rich, bromine poor environment. [19,20] As such, the most thermodynamically favorable defect that can form is excess lead on the surface of the nanocrystal. [19,20] This excess lead can be etched away through use of thiocyanate salts, such as NH₄SCN, increasing the CsPbBr₃ PLQY to within error of unity. [21,22] It is this high photoluminescence efficiency that makes CsPbBr₃ nanocrystals particularly promising for investigating optical applications and phenomena such as luminescence up-conversion.

1.2. Multi-photon Luminescence Up-conversion

Luminescence up-conversion is the process whereby a material converts lower energy absorbed photons into higher energy emitted photons. This optical process has applications in bioimaging, [24] as well as optical energy conversion where up-conversion can be utilized to decrease band-gap and thermalization losses. [25,26] For the sake of conservation of energy, the up-conversion mechanism often requires multiple absorbed photons for every emitted up-converted photon. In the simplest case, a carrier absorbed a photon and is excited to a metastable intermediate state; subsequently, the photoexcited carrier absorbs a second photon and is promoted into a higher energy state before relaxing radiatively, emitting a photon with energy no greater than the sum of the two absorbed photons. [23,24] These multi-photon up-conversion mechanisms have

drawn interest for their applications in bioimaging, [24] as well as in optical energy conversion. [25,26]

Most commonly, multi-photon up-conversion is accomplished using rare-earth metal doped dielectric materials. The 5f orbitals of these rare-earth metals provide a multitude of atomic transitions that can be utilized for a host of energy transfer mechanisms, ultimately pooling energy into a single excited carrier that will radiatively relax. Additionally, the 4p and 4s orbitals shield the 5f orbitals so that the energy transfer and emission mechanisms are not dependent on the chemical environment or the size of the host dielectric. [23,24] This method of up-conversion, however, has several drawbacks such as a lack of spectral tunability, low absorption cross-sections, and low quantum efficiency. Rare-earth metal up-conversion is typically has PLQY of only a few percent. [27] Alternative mechanisms, such as using dye-sensitization, can increase the efficiency to 20%, [28] but these methods suffer from a small number of applicable dye-sensitizer molecules, further reducing the general applicability of this method as well as the spectral tunability.

The ability to up-convert multiple low-energy photons into one higher energy photon is not limited to rare-earth metal dopants. In recent years, semiconductors, especially semiconducting nanocrystals, have been studied for their potential applications in luminescence up-conversion due to their size and morphology dependent emission lending spectrally tunable up-conversion, as well as their high photoluminescence efficiency. [29–33] Multi-photon up-conversion has been observed in a number of nanoparticle morphologies, with several different methods employed to

improve its efficiency, from adding a dopant intermediate state [34] to synthesizing multi-component nanocrystals with energy levels designed to promote up-conversion. [32,33]

Of this latter category, metal-semiconductor heterostructures have attracted some interest. One mechanism that has been proposed is hot-carrier luminescence up-conversion. [35,36] This method utilizes the hot carriers generated by plasmon decay in the metal to drive photoluminescence in the semiconductor. So long as the barrier for injecting hot-carriers from the metal into the semiconductor is lower in energy than the band-gap of the emitting semiconductor, the resulting emission will be higher in energy than the absorbed photons that drive the process. Initial calculations have suggested that this mechanism theoretically could occur with efficiency as high as 25%, where 50% efficiency would be the absolute thermodynamic limit due to the mechanism being a two-photon up-conversion process. [35,36]

While hot-carrier luminescence up-conversion was demonstrated in 2015 using lithographically prepared quantum well heterostructures, [36] further demonstration has not been forthcoming, likely due to the challenges in applying metal-semiconductor heterostructures to optical applications requiring fluorescence. Generally, metals that are in interface with a semiconductor entirely quench the fluorescence of said semiconductor [37] through charge separation across the interface, [38,39] exciton-plasmon coupling, [40,41] as well as the formation of defect states along the interface that can act as loss pathways. [41] As is discussed in Chapter 2, CsPbBr₃ perovskite nanocrystals are a promising material for overcoming this hurdle, as Au-CsPbBr₃ heterostructures have

been demonstrated to emit with up to 70% efficiency, [42–44] in stark contrast to the complete quenching of photoluminescence that is more typical in metal-semiconductor heterostructure nanocrystals.

1.3. One Photon Luminescence Up-conversion

While the most commonly studied form of up-conversion utilizes multiple absorbed photons, there is interest in the alternative one photon up-conversion luminescence. [45–48] In this, one lower energy absorbed photon is combined with several phonons to drive higher energy emission. This is the direct inverse process to Stokes shifted photoluminescence (SSPL) in which a higher energy photon is absorbed, some of that energy is lost as heat, and a lower energy photon is emitted. As such, it can be thought of as anti-Stokes photoluminescence (ASPL). Remarkably, if ASPL occurs with a high efficiency, the phonon modes of the emitting material may be depopulated leading to a net decrease in temperature, so called laser cooling or optically driven cooling. [45–47,49,50] It is this potential for laser cooling that drives interest in researching materials that demonstrate efficient ASPL.

As with multi-photon up-conversion, rare-earth metal doped dielectrics have garnered extensive research for ASPL cooling. [46,47,51] In Yb^{3+} , the most common rare-earth metal used for ASPL cooling, the crystal field of nearby ions in the host material lifts the degeneracy of the $^2F_{7/2}$ ground state and the $^2F_{5/2}$ excited state via the Stark effect. This leads to two manifolds of closely spaced electronic states such that intra-manifold thermal excitation can occur in the excited state manifold. Thus, optical excitation is followed by thermal excitation before radiative recombination. This

mechanism has been used to show the successful cooling of a number of different host materials. [46] Perhaps most notably, in 2016 Yb^{3+} doped YLiF_4 was cooled down to 91K via Yb^{3+} ASPL. [51] This is approximately the thermodynamic limit for rare earth metal cooling.

As a consequence of Boltzmann statistics, below 100 K the top electronic state of the ground-state manifold is depopulated, drastically decreasing the cooling efficiency and thus limiting cooling beyond 100 K. [45] The ground state population distribution of semiconductors, on the other hand, is governed by Fermi statistics. As such, the thermodynamic limit of semiconductor ASPL driven cooling is $< 10\text{K}$, at which point the rate of phonon-carrier interaction is slower than radiative recombination and it becomes unlikely that a photoexcited carrier will gain energy from a phonon prior to relaxation. [45]

The mechanism of semiconductor ASPL is currently not well understood. In the simplest terms, a narrow population of carriers is photoexcited using monochromatic excitation, such as a laser. This narrow distribution of carriers broadens as they equilibrate with the temperature of the semiconductor lattice, and then they radiatively relax. If the average energy of the carriers post-thermalization is greater than the average energy of the initially photoexcited distribution, then it is up-conversion as the emitted photons are, on average, shorter wavelength than the pump. [46]

While this works as a general description of semiconductor ASPL, the specifics of the mechanism are still uncertain, especially with regards to the existence and nature of an intermediate state. [52–56] There is debate in the literature as to the identity of the

state into which carriers are initially photoexcited. The prevailing view is that an electronic state acts as an intermediate, giving the photoexcited carriers some finite lifetime with which to couple to a phonon and be promoted into the semiconductor bands prior to relaxation. [54–56] It has been suggested that this electronic state is part of the exponential low energy tail of states at the bottom of the conduction band or is tied to some mid-gap defect state due to crystalline imperfections in the semiconductor. [52] This later description is especially prevalent in literature describing semiconducting nanocrystals ASPL, suggesting that the imperfect surfaces of nanocrystals give rise to mid-gap defect states that acts as the intermediate state for ASPL. [54–56] Recent studies have questioned these hypotheses, with some studies suggesting that the intermediate state, at least in some materials, could be self-trapped exciton, or even a virtual state rather than a real electronic state. [53,57,58]

While the thermodynamics governing the ground state population distribution of semiconductors favors ASPL cooling to cryogenic temperatures, experimental realization of ASPL cooling have not been forthcoming. This is due to the high fluorescence efficiency requirement for the thermal energy removed through ASPL to overcome the thermalization losses inherent in imperfect photoluminescence, as described in equation 1.1. [45]

$$P_{net} = \eta_e BN^2(h\nu - h\nu_e) + ANh\nu + CN^3h\nu_e + \Delta P \quad (1.1)$$

P_{net} is the net power deposited or removed from the semiconductor, with a negative value indicating cooling. The recombination processes are nonradiative (AN), radiative (BN^2) and Auger (AN^3). ΔP captures any other optical process that may

contribute energy to the semiconductor, such as parasitic or background absorption. The key parameters for achieving negative P_{net} are the external quantum efficiency (η_e) and the difference between the absorbed photon energy ($h\nu$) and the emitted photon energy ($h\nu_e$). For cooling to occur, the energy removed through ASPL, $\eta_e BN^2(h\nu - h\nu_e)$, has to be greater than the energy deposited in the semiconductor through other radiative pathways. The challenge is that the energy removed per up-converted photon is on the order of 100 meV, while the energy lost through nonradiative recombination is on the order of several eV. Thus, the external quantum efficiency (EQE) has to near unity for cooling. The exact efficiency required depends on $(h\nu - h\nu_e)$, which is the thermal energy removed per up-converted photon. For example, assuming ΔP is 0, if 20 meV of thermal energy is removed per up-converted photon, an EQE of greater than 99.2% is required to overcome the thermal energy of nonradiative recombination and drive cooling. If 80 meV of thermal energy is removed per up-converted photon, the EQE has to be greater than 96.7%.

GaAs has been extensively studied for its potential in ASPL cooling due to its internal quantum efficiency (IQE)—up to 99.7% in the case of AlGaAs/GaAs/AlGaAs double heterostructures. [59] While GaAs has IQE above the requisite efficiency threshold for cooling, its EQE is below said threshold—only 72% in the case of the AlGaAs/GaAs/AlGaAs double heterostructures. For thermal energy to be removed from the material system via ASPL, radiative recombination has to result in a free space photon. Every radiative recombination in GaAs, however, does not result in such a photon: Total internal reflection in the bulk semiconductor geometry can result in

radiative recombination that produces a photon that is reabsorbed by the semiconductor before it can escape into free space.

This loss is inherent to the bulk morphology of the GaAs films. Semiconductors that are sub-wavelength in size in at least one dimension do not have a significant difference between their IQE and EQE. This lack of total internal reflection was the insight that allowed Xiong and co-workers to demonstrate the first instance of semiconductor ASPL cooling, taking advantage of the sub-wavelength thickness of CdS nanobelts to cool them by 40 degrees. [50] Several years later, Xiong and co-workers similarly demonstrated the cooling of hybrid organic-inorganic perovskite thin films, once again sub-wavelength in thickness. [49] To date, Xiong and co-workers are the only researchers to report the successful cooling of a semiconductor via ASPL, despite several efforts to reproduce their results, a fact that has generated some controversy. [55,60]

As discussed in section 1.1, CsPbBr₃ perovskite nanocrystals have reproducibly been synthesized with PLQY approaching unity, after a facile NH₄SCN surface treatment. [21,22] This high PLQY, as well as their sub-wavelength size, has made them a potential target for ASPL cooling. Initial studies have been promising. CsPbBr₃ demonstrate efficient ASPL, emitting as much as 250 meV of thermal energy per up-converted photon. [53] These two characteristics make CsPbBr₃ an ideal material for studying ASPL, especially with the aim of potentially driving cooling.

2. GOLD DEPOSITION ON CESIUM LEAD TRIBROMIDE NANOCRYSTALS*

2.1. Introduction

As discussed in Section 1.1, CsPbX₃ perovskite nanoparticles show narrow emission linewidths with PLQY exceeding 80% that can be spectrally tuned by controlling the ratio of lead halide salts during synthesis, as first demonstrated by Protesescu et al. [1] Additionally, spectral tunability can be achieved post-synthetically with anion exchange reactions at temperatures as low as 60 °C. Remarkably, this exchange occurs even when nanocrystals with different halide compositions are in solution together at room temperature, whereby each nanoparticle acts as a halide source and labile oleylamine from the ligand shell transports halides through solution. [11,12,14] Similarly, van der Stam et al. [61] reported that divalent metals may undergo cation exchange reactions with cesium lead trihalide perovskites at room temperature, replacing up to 10% of the Pb cations present in the original perovskite with an isovalent metal. Their work suggested that complete cation exchange was not possible using divalent metals due to the limited metal cation mobility, and thus this technique was limited to doping the perovskite nanocrystals.

It was demonstrated by Balakrishnan and Kamat that gold can be deposited onto the surface of CsPbBr₃ nanocrystals via the reduction of Au salts by the nanocrystal surfactant shell. [42] As with similar Au-chalcogenide hybrid nanostructures, [62–64]

* Part of this chapter, including all figures and tables, is reprinted with permission from “Au Exchange or Au Deposition: Dual Reaction Pathways in Au–CsPbBr₃ Heterostructure Nanoparticles” by Benjamin J. Roman, Joseph Otto, Christopher Galik, Rachel Downing, and Matthew Sheldon, 2017. Nano Letters, 17, 5561–5566, Copyright 2017 by the American Chemical Society.

the metal domains can act as electrical contact points for nanoscale optoelectronic devices [65] or provide improved catalytic activity. [66] Additionally, plasmon-exciton coupling can modify the optoelectronic behavior and excited state dynamics of the heterostructure. [41,67] Using the nanocrystal surface ligands as reducing agents, however, compromises colloidal stability. Thus, the size of deposition was limited in this initial report and could not be increased beyond a diameter of 2 nm by the simple increase of Au ion concentration in solution. Additionally, as I show below, under these unstable synthetic conditions, a major side reaction is the uncontrolled exchange of Au^{3+} and Au^{1+} with Pb^{2+} ions in the perovskite nanocrystal lattice. This exchange is evidenced by characteristic diffraction peaks and nearly fully quenched PL. The exchange reaction should be mitigated if high quality optical materials, or precise control over the morphology of the nanocrystal heterostructure is desired.

Here, I show that both reaction outcomes, either the exchange of metal cations or the deposition of Au metal, can be controlled and optimized separately. The central insight guiding this study is that the concentration ratio of Au and Pb ions in solution will kinetically determine which ion is preferentially driven into the nanocrystal lattice. When both AuBr_3 and PbBr_2 are added to the nanocrystal solution, excess Pb^{2+} competitively prevents cation exchange with Au ions. Instead, Au^{3+} is reduced by oleic acid and oleylamine and deposits as Au metal on the surface of the CsPbBr_3 nanocrystals. The domain size of the metal deposition increases monotonically with the concentration of AuBr_3 in solution. Under these conditions, there is no evidence of cation exchange, and the PLQY of the resulting Au- CsPbBr_3 heterostructures can reach

70%, a remarkably high fluorescence yield considering the complete quenching of PL in similar Au-chalcogenide heterostructure nanoparticles. [37]

Alternately, adding a high concentration of only AuBr₃ promotes conditions that favor complete cation exchange. The resulting product is Cs₂Au^IAu^{III}Br₆, a tetragonal mixed valence perovskite previously studied as a bulk crystal. [68] As has been identified for macroscopic crystals, [69] Cs₂Au₂Br₆ nanoparticles have a band gap absorption onset at 1.6 eV with a photoluminescence maximum at 812 nm. Additionally, I show that the molar ratio of PbBr₂ compared to AuBr₃ determines the kinetics of deposition versus exchange, rather than the total amount of lead present in the reaction solution. Understanding these reaction dynamics is the first step towards producing lead-free all-inorganic perovskites utilizing this strategy of post-synthesis cation exchange.

2.2. Methods

2.2.1. Synthesis of CsPbBr₃ Nanoparticles

Based on the synthesis first reported by Protesescu et al. [1]

2.2.1.1. Preparation of Cesium Oleate

Cs₂CO₃ (0.200 g), OA (0.624 mL), and ODE (10 mL) were added to a 25-mL 3-neck round bottomed flask and heated for 1 hour at 120°C under vacuum to dry. After 1 hour, the flask was put under argon and heated to 150°C until all the Cs₂CO₃ had reacted.

2.2.1.2. Synthesis of CsPbBr₃ Nanoparticles

PbBr₂ (0.069 g) and ODE (5 mL) were added to a 25-mL 3-neck round bottomed flask and heated under vacuum to 120 °C for 1 hour. The solution was then placed under

argon, and dried OAm (0.5 mL) and dried OA (0.5 mL) were injected to solubilize the PbBr_2 . The temperature increased to 180°C , and the Cs-oleate (0.4 mL) was swiftly injected. After 1 minute, the solution was cooled with an ice bath. The final solution was centrifuged at 3000 g-forces for 5 minutes and the supernatant was discarded. The precipitate was suspended in 2 mL hexane, and then centrifuged at 3000 g-forces for 90 minutes. The precipitate was discarded, and the supernatant was diluted to a concentration of $0.60\ \mu\text{M}$ or $0.30\ \mu\text{M}$ for the deposition and cation exchange reactions, respectively. The concentration was calculated using the molar extinction coefficient, as reported by De Roo et al. [15]

2.2.2. Gold deposition and cation exchange reactions

2.2.2.1. Preparation of PbBr_2 Stock Solution

PbBr_2 (0.069 g) was placed in a vial with ODE (5 mL), OA (0.3 mL), and OAm (0.3 mL). This solution was heated to between 120 and 150°C until it turned clear. It was then cooled and stored for later use.

2.2.2.2. Preparation of AuBr_3 Solution

AuBr_3 (22 mg) was solubilized in EtOH (0.2 mL), and then diluted with toluene (2 mL). Aliquots of this solution were further diluted with toluene for use in deposition and cation exchange reactions. The stock solution was never stored for longer than an hour.

2.2.2.3. Cation Exchange Reaction

The desired amount of the AuBr_3 stock solution was diluted to a volume of 0.5 mL with toluene (i.e. 0.2 mL of the stock solution were diluted with 0.3 mL of toluene).

0.5 mL of the 0.30 μM CsPbBr₃ solution was placed in a vial with a stir bar. The AuBr₃ solution was swiftly injected, and the solution was left to stir overnight (16 hours). To clean, the solution was centrifuged at 3000 g-forces for 10 minutes. The perovskites are more soluble in the toluene/hexane solution than the AuBr₃, and so the supernatant was kept for further analysis.

2.2.2.4. Gold Metal Deposition Reaction

The desired amount of the AuBr₃ stock solution was diluted to a volume of 0.5 mL with toluene (i.e. 0.2 mL of the stock solution were diluted with 0.3 mL of toluene). 0.5 mL of the 0.60 μM CsPbBr₃ solution was placed in a vial with a stir bar. 19 μL of OA and 36.6 μL of the PbBr₂ stock solution were added to the AuBr₃ aliquot per 0.1 mL of the AuBr₃ stock solution used. This solution was stirred for 30 seconds, and then swiftly injected into the CsPbBr₃ solution. To clean, the volatile solvents were evaporated under nitrogen flow until only the oily OA and OAm remained, and 0.5 mL of ODE was added. The solution was centrifuged at 1300 g-forces for 5 minutes. The perovskites are less soluble in the ODE than the PbBr₂ and AuBr₃, and so the supernatant was discarded, and the precipitate was suspended in 1 mL of hexane for further analysis.

2.2.2.5. Finding the Minimum PbBr₂ to AuBr₃ Molar Ratio

The desired amount of the PbBr₂ solution was added to 0.5 mL of the AuBr₃ stock solution and stirred for 30 seconds. This solution was swiftly added to 0.5 mL of the 0.3 μM CsPbBr₃ solution and stirred for 30 seconds. The solution was then cleaned in the same manner as with the gold metal deposition reaction (see above).

2.2.3. Characterization Methods

2.2.3.1. Absorbance

UV-VIS spectra from 300 to 800 nm were collected on an Ocean Optics Flame-S-UV-Vis spectrometer with an Ocean Optics DH-200-Bal deuterium and halogen lamp light source. UV-Vis-NIR spectra from 500 to 1500 nm were collected on a Hitachi U-4100 UV-Vis-NIR spectrophotometer with a tungsten lamp.

2.2.3.2. Photoluminescence

PL was measured on a PTI QuantaMaster spectrofluorometer with a xenon arc lamp for steady state excitation. The emission was detected using a PMT (Hamamatsu R928). The fluorescence quantum yield (QY) was calculated relative to a Rhodamine 6g standard ethanol solution with a QY of 81%, calibrated using a Fluorescein standard.

2.2.3.3. Lifetime Measurements

Lifetime was measured using a 375 nm LED light source with 1.5 ns pulse width as the excitation source. The time-dependent luminescence intensity was recorded with a PMT (R928, Hamamatsu) using a time-domain stroboscopic detection method patented by PTI.

2.2.3.4. Transmission Electron Microscopy

TEM images were collected on a FEI Tecnai G2 F20 ST FE-TEM microscope operated at 200 kV

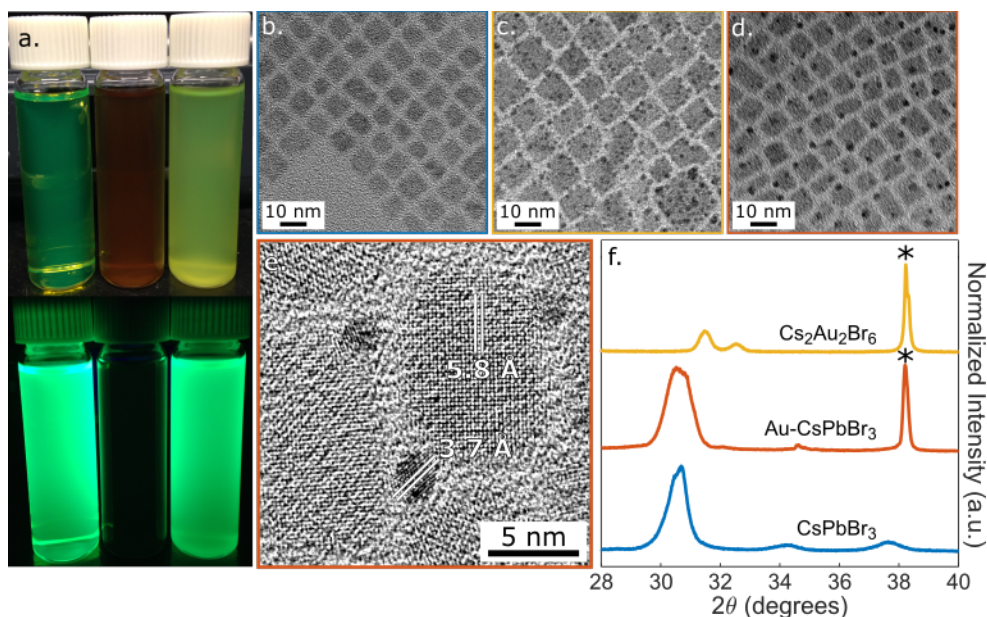


Figure 2.1: (a) Picture of CsPbBr₃ (left), Cs₂Au₂Br₆ (middle) and Au-CsPbBr₃ (right) in white light (top) and UV excitation (bottom). (b) TEM of CsPbBr₃. (c) TEM of CsPbBr₃ after gold cation exchange. (d) TEM of CsPbBr₃ with gold deposition. (e) TEM of Au-CsPbBr₃ heterostructures showing lattice spacings corresponding to the (202) plane of orthorhombic CsPbBr₃ (5.8 Å) and the (100) plane of cubic Au (3.7 Å). (f) Powder x-ray diffraction (XRD) diffractogram of CsPbBr₃ (blue trace), CsPbBr₃ with 3.0 nm deposition (orange trace), and the Cs₂Au₂Br₆ exchange product (yellow trace). A characteristic section of the diffractogram is shown. The visible peaks correspond to the (040) and (202) planes of both orthorhombic CsPbBr₃ and tetragonal Cs₂Au₂Br₆. The asterisk denotes the peak characteristic of the (111) plane of cubic gold.

2.2.3.5. Energy Dispersive X-Ray Spectroscopy

EDS spectra were collected on a FEI Tecnai G2 F20 ST FE-TEM microscope using a Fischione ultra-high resolution STEM HAADF detector coupled with an EDAX instruments EDS detector.

2.2.3.6. Powder X-Ray Diffraction

XRD measurements were taken with a Bruker-AXS D8 Advanced Bragg-Brentano diffractometer equipped with Cu K- α x-ray radiation and a Lynxeye position sensitive detector.

2.3. Results and Discussion

Figure 2.1 summarizes the major differences between the reaction products of Au metal deposition versus Au cation exchange. Figure 2.1a shows suspensions of CsPbBr₃ nanocrystals as synthesized (left) and after reacting with AuBr₃, without and with excess PbBr₂ (middle and right, respectively). The difference is stark, both under ambient lighting (top), and under UV lamps (bottom). When viewed using TEM, however, the two products are not as obviously distinct. Figure 2.1b shows an unreacted sample of CsPbBr₃ nanocrystals appearing as cuboids with edge lengths of about 8 to 10 nm. Figures 2.1c and 2.1d show the same batch of CsPbBr₃ after reaction with a 0.5 mL of a 13.74 mM AuBr₃ solution, without and with the inclusion of PbBr₂ in the reaction solution, respectively. Both samples appear as cuboid nanoparticles with points of contrast that have a lattice spacing resolvable by HRTEM corresponding to cubic gold (Figures 2.1e). It is important to emphasize that TEM alone cannot confirm the presence or lack of the exchange product, and thus careful x-ray diffraction (XRD) structural analysis is necessary to characterize the product.

Figure 2.1f highlights the structural differences in the XRD diffractograms for CsPbBr₃ (blue trace), Au-CsPbBr₃ (orange trace), and Cs₂Au₂Br₆ (yellow trace). The visible peaks correspond to the (040) and (202) planes of both orthorhombic CsPbBr₃

and tetragonal $\text{Cs}_2\text{Au}_2\text{Br}_6$, while the peak with the asterisk corresponds to the (111) lattice plane of cubic gold, indicating that gold nanoparticles are present in both solutions. Due to the difficulty in cleaning these samples, a large amount of gold is in solution that is not on the surface of a perovskite. As such, the sharp (111) cubic Au peak include contributions both from gold on and off the surface of a nanoparticle. In the sample with PbBr_2 added, both CsPbBr_3 and cubic Au appear on the diffractogram. The

Table 2.1: Perovskite nanocrystal optical properties due to Au metal deposition or Au cation exchange

AuBr ₃	QY at 510 nm	Amplitude Averaged Lifetime	Deposition Diameter
before	60.01%	5.25 ns	--
0 mM	74.15%	10.05 ns	--
4.58 mM	70.18%	10.11 ns	2.5 ± 0.5 nm
13.74 mM	51.36%	6.27 ns	2.7 ± 0.6 nm
22.90 mM	11.26%	3.82 ns	3.0 ± 0.7 nm
4.58 mM, no PbBr_2	1.64%	< 1.00 ns	--

cation exchange sample, however, has major peaks characteristic of a tetragonal $\text{Cs}_2\text{Au}_2\text{Br}_6$ perovskite crystal structure, as discussed below.

Remarkably, CsPbBr_3 retains high PLQY when Au metal nanoparticles are deposited and when no cation exchange has occurred, as demonstrated in Table 2.1 and Figure 2.2. The values reported in Table 2.1 for ‘before’ correspond to CsPbBr_3 as synthesized. The values reported for 0 mM AuBr₃, however, correspond to a control

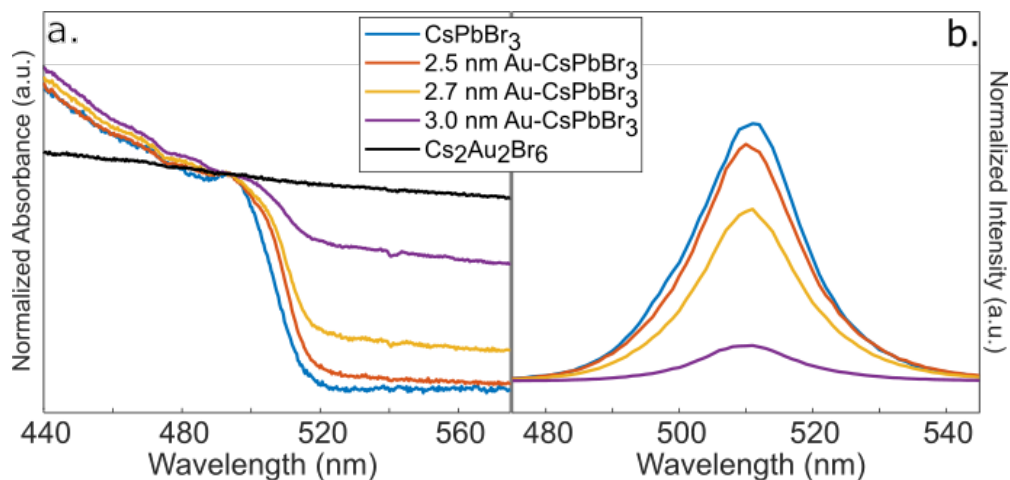


Figure 2.2: (a) Absorbance of CsPbBr₃ before and after Au metal deposition compared to the cation exchange product, Cs₂Au₂Br₆. (b) Photoluminescence of CsPbBr₃ before and after Au metal deposition, normalized to 510 nm PLQY.

sample wherein PbBr₂ and oleic acid were added to 0.5 mL of the CsPbBr₃ solution as if performing a 22.90 mM AuBr₃ deposition. This reaction shows that the inclusion of oleic acid and oleylamine to solubilize the PbBr₂ is not responsible for the observed decrease in quantum yield and fluorescent lifetime. Instead, including small amounts of oleylamine and oleic acid increases the fluorescent quantum yield and lifetime, as has been reported by De Roo et al., who suggested that this effect, brought about by the addition of oleylamine, is due to a larger fraction of tightly bound oleate on the surface of the nanocrystals. [15]

As shown in Table 2.1 and Figure 2.2b, Au deposition decreases the fluorescence quantum yield and fluorescent lifetime. Similarly, the CsPbBr₃ band edge absorbance (Figure 2.2a) becomes less distinct, and the absorbance tail to the red increases with increasing Au solution concentration, as has been observed previously on many hybrid

gold-nanoparticle structures. [42,64] These changes in optical properties can be attributed to the modification of the perovskite electronic structure by the gold metal region. With the inclusion of PbBr₂ to prevent any Au cation exchange, these effects increase monotonically with the concentration of the gold precursor solution. Statistical analysis on TEM images reveals that the average diameter of deposited Au nanoparticles increases with increasing AuBr₃ solution concentration, from 2.5 ± 0.5 nm to 3.0 ± 0.7 nm, as reported in Table 2.1. This change in size can explain the monotonic decrease in PLQY and lifetime.

At the smallest deposition size studied (2.5 ± 0.5 nm), the PLQY at 510 nm is still high, at 70.18%, a result that is striking when compared with similar hybrid Au-chalcogenide nanoparticle heterostructures for which complete quenching of photoluminescence has been observed. [37] Maintaining such high PLQY while in contact with the metal deposition regions, along with the ability to tailor the optical coupling via control of the Au metal deposition size, suggests that Au-CsPbBr₃ nanoparticles may offer new opportunities for optoelectronic device applications in comparison with other metal-semiconductor heterostructure nanoparticles. Determining the reason for the high fluorescence PLQY while still in contact with a metal will require further study. However, Lorenzon et al. published a report [70] that suggests that CsPbBr₃ is more sensitive to hole traps than electron trap states, and the removal of localized surface electrons can thus lead to an increase in fluorescent PLQY. It is possible that these surface electrons are being injected into the Au metal, and the

resulting increase in PLQY partially counterbalances the usual fluorescent quenching of the semiconductor by the metal.

However, for the same concentration of AuBr_3 without the addition of PbBr_2 the PL at 510 nm was severely or completely quenched. To study this behavior, I performed an AuBr_3 concentration study of the cation exchange reaction. 0.5 mL of AuBr_3 solutions with varying concentrations were added without PbBr_2 to 0.5 mL of the 0.30 μM CsPbBr_3 solution and allowed to stir overnight (16 hours). During the first few minutes of the reaction, the solution turned from green to dark brown rather than the

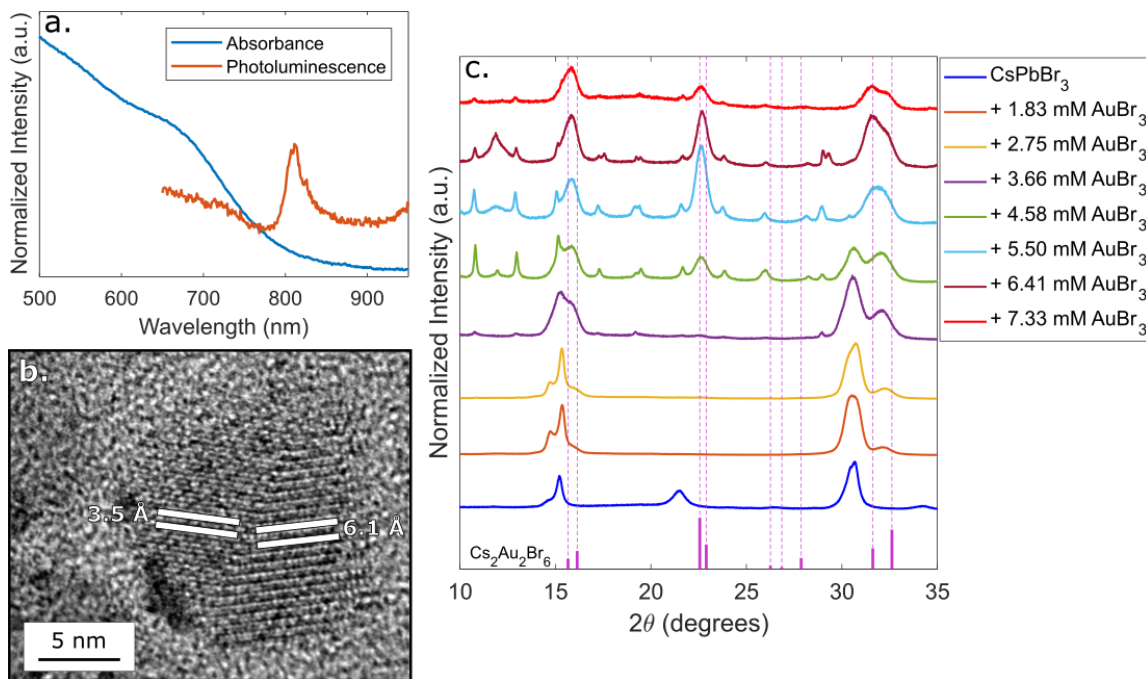


Figure 2.3: (a) Spectra showing the normalized absorbance and photoluminescence of $\text{Cs}_2\text{Au}_2\text{Br}_6$. (b) HRTEM image showing a partially exchange nanocrystal. Resolved lattice spacings correspond with the (202) plane of orthorhombic CsPbBr_3 and the (103) plane of tetragonal $\text{Cs}_2\text{Au}_2\text{Br}_6$. (c) Normalized XRD diffractograms showing the progression of cation exchange as 0.5 mL AuBr_3 solutions with increasing concentration are added to identical amounts of CsPbBr_3 .

light orange color observed during Au metal deposition. This distinct color change is the first indication that cation exchange has occurred.

Before reaction with AuBr₃, the diffractogram of CsPbBr₃ nanocrystals closely matches the orthorhombic crystal structure determined by Cottingham et al [71] (Figure 2.3c; bottom, dark blue plot). When a solution containing AuBr₃ is added to the CsPbBr₃ solution, some Au³⁺ exchanges with Pb without being reduced by the oleylamine ligand shell, some is reduced to Au⁺ before exchanging with Pb, and some is reduced to Au⁰ metal nanoparticles and deposits on the surface of the nanocrystals. Figure 2.3c shows the structural evolution of this cation exchange process as solutions of increasing AuBr₃ concentration are added to identical solutions of CsPbBr₃. As solutions with increasing AuBr₃ concentration are added, diffraction peaks characteristic of Cs₂Au₂Br₆ grow in with peak positions matching those reported by Matsushita et al. [68] Additionally, individual crystals with domains of both CsPbBr₃ and Cs₂Au₂Br₆ can be identified using TEM, as determined using resolved lattice spacing (Figure 2.3b). Half of the nanocrystal has lattice spacing of about 3.5 Å, approximately corresponding to the (103) lattice plane of Cs₂Au₂Br₆. The other half of the crystal has lattice spacing of about 6.1 Å, approximately corresponding to the (202) lattice plane of CsPbBr₃. Trap states due to defects along the interface between the Cs₂Au₂Br₆ and the CsPbBr₃ domains may lead to the severe quenching of 510 nm photoluminescence when partial cation exchange has occurred.

When a 7.33 mM AuBr₃ solution is used, CsPbBr₃ peaks are no longer present in the diffractogram of the final product, indicating that Pb has been completely exchanged for Au to produce entirely Cs₂Au₂Br₆. The complete exchange of Pb for Au was confirmed using energy dispersive x-ray spectroscopy, in which no Pb signal was measured (Figures 2.4). As has been reported for the bulk structure, [69] I measured a band gap absorption onset at about 1.6 eV, with an asymmetric photoluminescence with a maximum at 812 nm (Figure 2.3b). Raman scattering was removed from the photoluminescence spectrum shown in Figure 2.3b. The broad band edge and asymmetric photoluminescence are likely due to the polydispersity of the sample produced using cation exchange, as well as the presence of metallic Au nanoparticles on

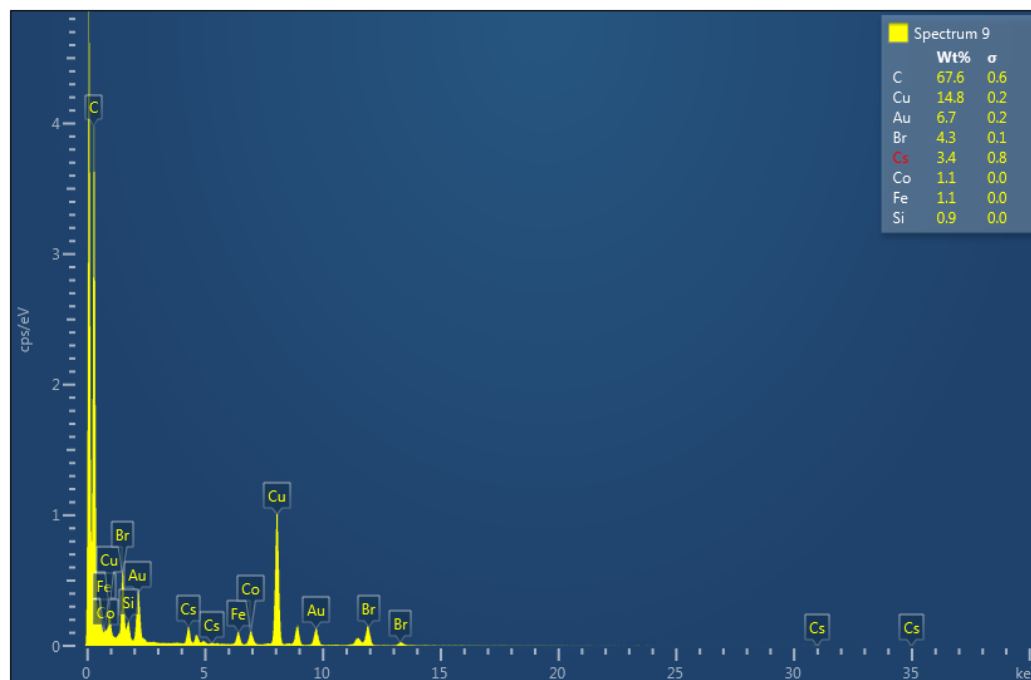


Figure 2.4: Energy dispersive x-ray spectrum demonstrating the absence of Pb after the cation exchange reaction of AuBr₃ with CsPbBr₃.

the surface of the $\text{Cs}_2\text{Au}_2\text{Br}_6$ nanoparticles. Based on a statistical analysis of TEM images, the metallic Au nanoparticles on the surface of the complete cation exchange product have a diameter of 3.54 ± 2.45 nm. They are, on average, larger than the Au nanoparticles in the samples where PbBr_2 was added to prevent cation exchange, but their size also varies significantly.

To better understand the amount of PbBr_2 needed to prevent cation exchange, I performed a series of Au depositions (0.5 mL of 7.33 mM AuBr_3 solution added to 0.5 mL of 0.3 μM CsPbBr_3 solution, see Section 2.2.2), adding varying amounts of the PbBr_2 solution to each, and then measured powder XRD of the final products, looking for signs that cation exchange had occurred. Estimating the number of Pb^{2+} cations per nanoparticles to be approximately 3600 (0.2 nm^3 unit cell, 729 nm^3 nanocrystal volume), I consider the molar ratio of Au to Pb in solution, separately analyzing the Pb present in the nanocrystals as well as the added PbBr_2 . The results are summarized in Table 2.2. There is no evidence of cation exchange until the Au concentration is at least 4.4 times larger than the total Pb concentration, accounting for both the Pb from the nanocrystal lattice and the added PbBr_2 salt. However, as is listed in the bottom row of Table 2.2, this Au:Pb molar ratio is 5 times larger than the sample with earliest indication of cation exchange in Figure 2.3c, when no additional PbBr_2 salt is included in the reaction. Thus, PbBr_2 is necessary in solution to prevent cation exchange from occurring.

Table 2.2: Au:Pb molar ratio dependence of cation exchange.

CsPbBr ₃ (μ moles)	PbBr ₂ (μ moles)	AuBr ₃ (μ moles)	Au:Pb	Au:PbBr ₂	Cation Exchange?
1.08	3.08	11.45	2.75	3.72	No
1.08	2.31	11.45	3.38	4.96	No
1.08	1.54	11.45	4.37	7.44	Yes
1.08	0.77	11.45	6.19	14.87	Yes
1.08	0.00	0.92	0.85	--	Yes

2.4. Conclusions

Nanocrystals of pure Cs₂Au₂Br₆ represent a new all-inorganic halide perovskite nanocrystal achieved via a post-synthetic cation exchange reaction strategy and are the first example of an all-inorganic perovskite nanocrystal achieved via a complete cation exchange reaction. Given the unique optical properties of all-inorganic halide perovskite nanocrystals, there have been efforts to synthesize lead-free cesium halide perovskites by utilizing tin, [72,73] bismuth, [74] and antimony [75] precursors. Post-synthetic methods of metal cation exchange, like reported here, may enable study of the unique optoelectronic properties of a wide variety of all-inorganic perovskite nanocrystals without sacrificing the simple hot injection method used to synthesize monodisperse CsPbX₃. In addition, cation exchange reactions can provide a new strategy in the search for less toxic alternatives to lead-based perovskites.

Most notable about the Au-CsPbBr₃ heterostructure nanocrystals is their high PLQY, up to 70% with 2.5 nm gold deposition. This is remarkable considering the

complete quenching of PL that is typically observed for metal-semiconductor nanoparticle heterostructures. [37] This opens up new opportunities for utilizing these metal-semiconductor heterostructures in optical applications where efficient photoluminescence is required, such as hot-electron luminescence up-conversion. [35,36]

In summary, Au metal deposition or Au cation exchange with CsPbBr₃ may be achieved controllably via the addition of AuBr₃ with or without excess PbBr₂, respectively. Cs₂Au₂Br₆, the cation exchange product, is observable by XRD with a diffractogram corresponding to an orthorhombic crystal structure with Au atoms replacing Pb atoms. Additionally, the exchange product is optically active with a band gap absorption onset and photoluminescence in the NIR. Partially exchanged samples show a significant decrease in PL at 510 nm, even for low concentrations of Au ions. Au metal deposition, on the other hand, decreases the 510 nm fluorescence quantum yield and lifetimes monotonically with deposition size, which is tunable based on the Au precursor concentration, and is compatible with high QY of up to 70%.

3. THE ROLE OF MID-GAP STATES IN ONE PHOTON UP-CONVERSION*

3.1. Introduction

As discussed in Section 1.2, luminescence up-conversion is the process whereby a system absorbs low energy photons and emits higher energy photons. This phenomenon has a variety of applications, including biological imaging [76] and optical energy conversion. [77] The most commonly studied luminescence up-conversion mechanisms result from multi-photon processes, using rare earth dopants [23] or triplet-triplet annihilation. [78]

As is further discussed in Section 1.3, single photon up-conversion, also known as anti-stokes photoluminescence (ASPL), can result when the energy disparity between the absorbed low energy photon and the emitted high energy photon is provided by phonon scattering. [48] With sufficiently high quantum yield, this process can lead to a decrease in the phonon population of the system, for potential applications in optically driven cooling. Research efforts in this mechanism have largely focused on bulk semiconductors with two closely spaced excited states, separated by no more than a few kT . When electrons are resonantly excited into the lower energy excited state, it becomes overpopulated relative to the second excited state. Electrons from the first excited state then rapidly absorb phonons and populate the second excited state, leading to an increase in the average energy of the emitted photons.

* Part of this chapter, including all figures and tables, is reprinted with permission from “The role of mid-gap states in all-inorganic CsPbBr₃ nanoparticle one photon up-conversion” by Benjamin J. Roman and Matthew Sheldon, 2018. Chemical Communications, 54, 6851–6854, Copyright 2018 by the Royal Society of Chemistry.

While difficult to optimize in fabricated semiconductor devices, ASPL appears to be ubiquitous in quantum-confined colloidal nanomaterials and has been observed in a variety of nanoparticle morphologies including CdS nanobelts, [50,56] CdTe quantum dots, [79,80] InP quantum dots, [81,82] carbon quantum dots, [83] and CdSe quantum dots, with and without a ZnS shell [80,82] To explain the mechanism of ASPL in nanoparticles, it has often been suggested that mid-gap surface trap states play the role of the intermediate state necessary for up-conversion. In this model, the mid-gap state acts as the low-energy excited state, and the valence or conduction bands act as the second excited state, depending on whether the phonon is exciting the hole or electron, respectively. [54,56,84] This explanation, however, is called into question by the observation of ASPL in these nanocrystals, irrespective of their chemical makeup, or surface structure, with ASPL observable even in nanocrystal heterostructures with a passivating inorganic shell that removes the mid-gap trap states of the emitting core. Additionally, longitudinal optical phonon modes in nanocrystals are, on average, significantly lower in energy than observed anti-Stokes shifts, implying that a fundamentally different mechanism may be responsible for the ASPL that is commonly observed in nanocrystals. [48,85]

All-inorganic lead halide perovskite nanocrystals have recently been of great interest to the research community due to their favorable optical properties. Cesium lead trihalide perovskite nanocrystals, in particular, demonstrate high efficiency photoluminescence tunable across the entire visible spectrum.[1] Morozov and co-workers demonstrated ASPL in all-inorganic CsPbBr₃ perovskite nanoparticles, with

efficiencies up to 75%. [84] Soon after, Ye and co-workers demonstrated the energy dependence of ASPL in CsPbBr₂ mixed-halide nanocrystals, using the excitation wavelength-dependent change in ASPL intensity to probe the energy distribution of the mid-gap trap states in the perovskite nanocrystals that were presumed to be responsible for the observed ASPL. [54] In line with reports of other nanocrystal systems, they suggested a mechanism in which a photon with energy smaller than the band gap excites an electron from a continuum of trap states above the valence band edge into a surface-related mid-gap trap state below the conduction band edge. A subsequent phonon excitation drives the resulting hole into the valence band where it can radiatively recombine, giving off an up-converted photon.

With initial ASPL efficiencies as high as 75%, CsPbBr₃ nanoparticles are a promising materials system for study of optical cooling applications. Moreover, given the flurry of research activity since the first report of their synthesis, [1] there is a growing understanding that the very high efficiency of a variety of optical and optoelectronic processes in all-inorganic perovskite nanocrystals is in large part due to their tolerance to trap states, with most lying near, or inside of the valence or conduction bands. [19] This, however, seems at odds with the proposed mechanism for ASPL requiring long-lived mid-gap trap states that support phonon absorption. If efficient ASPL is to be accomplished utilizing all-inorganic perovskite nanocrystals, it is important for researchers to understand the role of mid-gap states in the up-conversion mechanism, either as a loss pathway or as a fundamental requirement of the mechanism.

Table 3.1: Summary of spectral data for above and below-gap excitation

	460 nm Excitation			532 nm Excitation			
	<i>Position</i>	<i>FWHM</i>	<i>PLQY</i>	<i>Position</i>	<i>FWHM</i>	<i>PLQY</i>	<i>E_a</i>
CsPbBr ₃	511 nm	103 meV	68%	518 nm	74 meV	11%	158 meV
SCN:CsPbBr ₃	508 nm	108 meV	100%	515 nm	69 meV	33%	151 meV

To this aim, I investigated the dependence of ASPL on CsPbBr₃ mid-gap states. CsPbBr₃ nanocrystals were treated with NH₄SCN to increase their PLQY from above-gap excitation to unity, producing nanoparticles essentially free of mid-gap states. [21] These NH₄SCN-treated nanoparticles show higher ASPL efficiency than their untreated counterparts, suggesting that mid-gap states constitute a loss pathway for ASPL, just as for conventional photoluminescence from above-gap excitation. Additionally, Arrhenius plots were constructed using the temperature dependence of ASPL to estimate the energy of activation (E_a) of the ASPL process. It is shown that the NH₄SCN treatment does not modify the E_a , indicating that significant changes to the mid-gap electronic structure do not alter the fundamental energetics of the ASPL process. Further, the E_a is significantly larger than the longitudinal optical phonon, [85] by approximately 130 meV, which implies that the up-conversion is mediated through a mechanism that is coupled to the background thermal bath of the crystal lattice rather than a specific excitation from an electronic state that is coupled to a single phonon. These results are summarized in Table 3.1.

3.2. Methods

3.2.1. Synthesis of CsPbBr₃ Nanoparticles

Based on the synthesis first reported by Protesescu et al. [1] NH₄SCN treatment follows the method first reported by Koscher et al. [21]

3.2.1.1. Preparation of Cesium Oleate

Cs₂CO₃ (0.200 g), OA (0.624 mL), and ODE (10 mL) were added to a 25-mL 3-neck round bottomed flask and heated for 1 hour at 120°C under vacuum to dry. After 1 hour, the flask was put under argon and heated to 150°C until all the Cs₂CO₃ had reacted.

3.2.1.2. Synthesis of CsPbBr₃ Nanoparticles

PbBr₂ (0.069 g) and ODE (5 mL) were added to a 25-mL 3-neck round bottomed flask and heated under vacuum to 120 °C for 1 hour. The solution was then placed under argon, and dried OAm (0.5 mL) and dried OA (0.5 mL) were injected to solubilize the PbBr₂. The temperature increased to 180°C, and the Cs-oleate (0.4 mL) was swiftly injected. After 1 minute, the solution was cooled with an ice bath. The final solution was centrifuged at 3000 g-forces for 5 minutes and the supernatant was discarded. The precipitate was dispersed in hexane.

3.2.1.3. NH₄SCN Treatment of CsPbBr₃ Nanoparticles

NH₄SCN was added to a vial of CsPbBr₃ suspended in hexane and vigorously stirred for between 20 and 30 minutes. The resulting cloudy solution was centrifuged at 3000 g-forces for 5 minutes, and the supernatant was decanted and analyzed.

3.2.2. Characterization Methods

3.2.2.1. Absorbance

UV-VIS spectra from 300 to 800 nm were collected on an Ocean Optics Flame-S-UV-Vis spectrometer with an Ocean Optics DH-200-Bal deuterium and halogen lamp light source. UV-Vis-NIR spectra from 500 to 1500 nm were collected on a Hitachi U-4100 UV-Vis-NIR spectrophotometer with a tungsten lamp.

3.2.2.2. Above-gap Excitation Photoluminescence (SSPL)

SSPL was measured on a PTI QuantaMaster spectrofluorometer with a xenon arc lamp for steady state excitation, using a holographic grating to select for 462 nm excitation. The emission was detected using a PMT (Hamamatsu R928). The photoluminescence quantum yield (PLQY) was calculated relative to a fluorescein standard with a PLQY of 95%. The excitation wavelength for PLQY measurements was 460 nm.

3.2.2.3. Below-gap Excitation Photoluminescence (ASPL)

ASPL was measured using a 532 nm Nd:YAG CW laser ported through a WITec alpha 300 RA confocal microscope, focused on the sample using a long working distance 0.55 numerical aperture objective. The solutions were analyzed in capped quartz cuvettes placed under the objective. The PLQY was calculated relative to a Rhodamine 6g standard with a QY of 95%. The absorbance of the samples at 532 nm was determined by measuring their transmission and using the relationship $A = \log_{10}(T)$.

3.2.2.4. Temperature Dependence of ASPL

Samples were sandwiched between two quartz slides and heated using a Linkam Instruments TS1500 thermal stage attached to the WITec alpha 300 RA confocal microscope.

3.2.2.5. Powder X-Ray Diffraction (XRD)

XRD measurements were taken with a Bruker-AXS D8 Advanced Bragg-Brentano diffractometer equipped with Cu K- α x-ray radiation and a Lynxeye position sensitive detector.

3.2.2.6. Energy Dispersive X-Ray Spectroscopy (EDS)

EDS spectra were collected on a FEI Tecnai G2 F20 ST FE-TEM microscope using a Fischione ultra-high resolution STEM HAADF detector coupled with an EDAX instruments EDS detector.

3.2.2.7. Transmission Electron Microscopy (TEM)

TEM images were collected on a FEI Tecnai G2 F20 ST FETEM microscope operated at 200 kV.

3.3. Results and Discussion

The optical characterization of CsPbBr₃ nanoparticles, with and without surface treatment, is displayed in Figure 3.1. As shown by the dashed lines in Figure 3.1a, NH₄SCN treatment blue shifts the PL resulting from above-gap excitation, i.e. the Stokes-shifted PL (SSPL), from 511 nm to 508 nm. As reported by Alivisatos and co-workers, [21] this results from a change in the nature of the emitting states due to the removal of excess Pb²⁺ from the nanoparticle surface. Excess Pb²⁺ is largely responsible

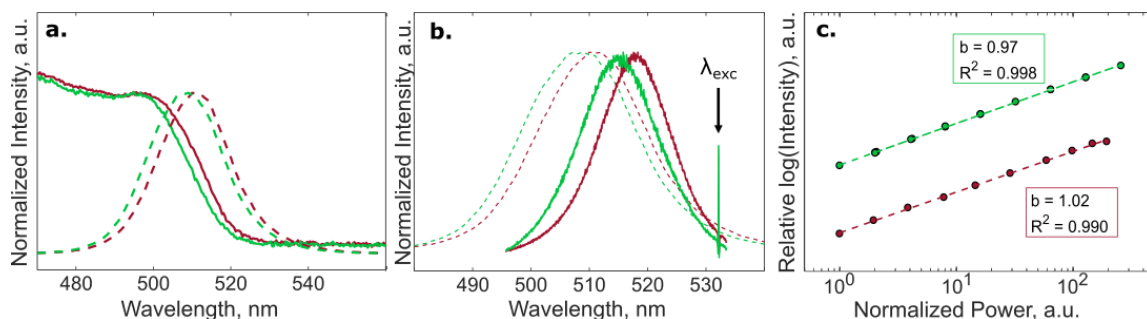


Figure 3.1: Optical characterization of CsPbBr₃, with (green) and without (red) NH₄SCN treatment. (a) Absorbance and above-gap excitation photoluminescence. (b) Photoluminescence under 460 nm (dashed) and 532 nm (solid) excitation. (c) Normalized log-log plot of the power dependence of CsPbBr₃ photoluminescence under 532 nm excitation.

for mid-gap states in the CsPbBr₃ nanocrystals. [19] The observation of unity quantum yield after the NH₄SCN treatment indicates near-complete removal of mid-gap trap states that provide non-radiative recombination pathways. The solid lines in Figure 3.1b show the up-converted photoluminescence resulting from 532 nm laser excitation.

The ASPL is systematically red shifted compared to the SSPL, with the ASPL maximums at 515 nm and 518 nm for NH₄SCN-treated and untreated samples, respectively. This systematic red shift is an ensemble effect due to the larger particles and lower energy emitters more strongly absorbing the light. As demonstrated by Morozov and co-workers, [84] single particle measurements show no spectral shift for ASPL, as compared to SSPL, confirming the observed red shift is a feature of the ensemble measurement, and that both SSPL and ASPL are produced through radiative recombination across the band gap. As with the SSPL, the ASPL from the NH₄SCN treated sample is also blue shifted from its unmodified counterpart, from 518 nm to 515

nm. This suggests that the ASPL emitting states are similarly modified by the NH₄SCN treatment.

Figure 3.1c shows the power dependence of the ASPL with and without NH₄SCN treatment, plotted on a log-log plot, normalized to their respective PLQY's. A linear fit reveals a slope of approximately 1 for both samples, which is indicative of a single photon process, as described by the relationship $PL \propto I^b$, where PL is the photoluminescence intensity, I is the excitation intensity, and b is the number of photons involved in the excitation process. This confirms that the up-conversion photoluminescence is, in fact, a single photon process.

The PLQY and full-width at half-maximum (FWHM) of the photoluminescence under 460 nm and 532 nm excitation is reported in Table 3.1. The FWHM of the photoluminescence is significantly narrower under 532 nm excitation when compared to 460 nm excitation. As discussed previously, this is only present in ensemble measurements and is due to larger particles and lower energy emitters preferentially absorbing the incoming radiation. Interestingly, the ASPL PLQY increases from 11% with unmodified CsPbBr₃ nanoparticles to 33% after NH₄SCN treatment. The increase in ASPL quantum yield suggests that the mid-gap states removed by the NH₄SCN surface treatment are, in fact, significant loss pathways. If mid-gap trap states were integral to the up-conversion mechanism, we would expect quenching of ASPL as the presence of these states are significantly diminished, or removed entirely, as indicated by the unity PLQY of the SSPL in the same sample. It is important to note that these values are limited by our ability to resolve the sample's below-gap absorption. Due to the low

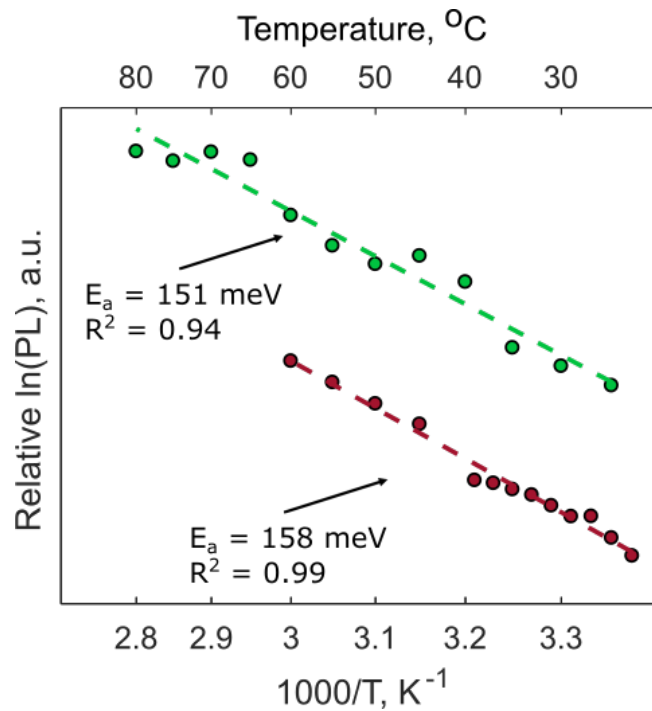


Figure 3.2: Arrhenius plots for CsPbBr₃, with (green) and without (red) NH₄SCN treatment.

absorption cross-section of the CsPbBr₃ nanoparticles at 532 nm, this measurement is noise limited, and thus the PLQY values reported in Table 3.1 represent the lower bounds of emission efficiency.

As the ASPL is thermally activated, the PL intensity is expected to increase with increasing temperature rather than the quenching of photoluminescence that occurs with temperature in multi-photon mechanisms of luminescent up-conversion. [48] Using an Arrhenius equation, $\ln(ASPL) \propto -E_a/kT$, I estimated the energy of activation for the ASPL mechanism. As demonstrated in Figure 3.2, the E_a for ASPL in CsPbBr₃ nanoparticles does not significantly change after NH₄SCN treatment, though the nanoparticles did appear to have greater thermal stability after treatment. Therefore, even if NH₄SCN does not entirely remove mid-gap trap states, but rather modifies the mid-

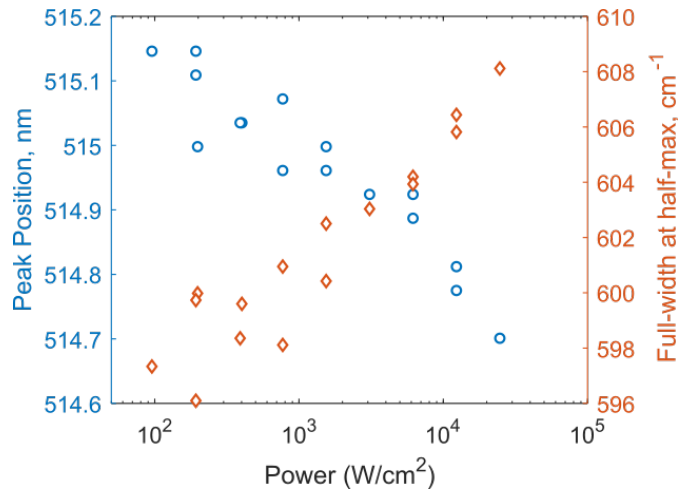


Figure 3.3: Power dependent spectral shift (blue circles, left axis) and broadening (orange diamonds, right axis) of NH₄SCN-treated CsPbBr₃.

gap energy level structure, this change to the energy landscape is not apparent in the E_a of the ASPL. Interestingly, the measured E_a (about 150 meV) is much greater than the average longitudinal optical phonon energy measured in CsPbBr₃ (about 20 meV). [85] Further, the anti-Stokes shift in energy is several times greater than the average optical phonon, with blue-shifts of 63 meV and 77 meV observed for the CsPbBr₃ without and with NH₄SCN treatment, respectively. This further suggests that the up-conversion is mediated through a mechanism that is coupled to the background thermal bath of the crystal lattice rather than a specific excitation from an electronic state that is coupled to a single phonon

It is interesting to note that the NH₄SCN-treated nanoparticles displayed a reversible blue shift and broadening of the ASPL monotonically with excitation power (Figure 3.3). Previous reports have ascribed this behavior to a distribution of hole trap states near the valence band edge. [54] However, this behavior is consistent with the

preferential absorption of incoming radiation by lower energy emitters discussed previously. As the excitation power density increases, lower energy emitters are saturated, leading to increasing emission from higher energy emitters. The ensemble nature of this phenomenon is further supported by single particle measurements showing no spectral shift or change in linewidth of ASPL as compared to SSPL. [84] Untreated CsPbBr₃ showed a more dramatic blue shift with increasing laser power, however this behavior was not reversible and seemed to be convoluted with lower photostability of those samples.

The apparent ubiquity of ASPL in quantum dots, regardless of their material or surface structure, suggests that the intermediate state may be intrinsic to nanoparticles. It has been previously suggested that the local electronic environment of the nanoparticle surface allows for exciton-polarons, enabling more effective coupling to optical phonons, even without mid-gap trap states. [48] Alternately, it has been suggested that excitons approaching the nanoparticle surface may be treated as a reaction coordinate in a semiclassical Marcus-Jortner model. [86] Within the framework of this analysis, excitons are more polarized due to the surface electronic environment, leading to greater Fröhlich interactions. Further study will be necessary to determine the nature of the vibrational coupling mechanism.

3.4. Conclusions

In conclusion, NH₄SCN surface treatment improves the efficiency of ASPL in CsPbBr₃ nanoparticles. This improvement in ASPL PLQY is believed to be due to the removal of mid-gap trap state loss pathways. The energy of activation of ASPL, as

estimated using an Arrhenius plot, is not significantly modified by the removal of mid-gap states. In combination with the magnitude of the activation energy of the ASPL process compared with the available phonon energy, this suggests that discrete mid-gap states coupled with single phonon excitations cannot explain the mechanism of quantum dot ASPL mechanism as previously proposed for all-inorganic perovskite nanocrystals.

[54]

4. OPTICALLY DRIVEN COOLING VIA ONE PHOTON UP-CONVERSION*

4.1. Introduction

As discussed in Section 1.3, if anti-Stokes photoluminescence (ASPL) occurs with an external quantum efficiency (EQE) near unity, more thermal energy is removed via ASPL than is added by thermalization due to nonradiative recombination, and the material will experience a net decrease in temperature. This mechanism of optically-pumped cooling, also called laser cooling, [45] has been demonstrated for a number of materials over the decades since it was first proposed. [87] Fluorescent dyes, for example, have been demonstrated to cool by several degrees during ASPL. [88–90] Most commonly, rare earth metal doped glasses are used for studying and demonstrating optical cooling, reaching temperatures as low as 91 K, [51] close to the thermodynamic limit of that material system. [46]

In comparison, semiconductors are theoretically predicted to be able to reach temperatures below 10 K via ASPL optical cooling; [45,91] despite this, optical cooling of bulk semiconductors has yet to be demonstrated. For net cooling to occur, the thermal energy scavenged by emitted photons—a few tens to a few hundreds of meV worth of energy for each emission event—has to be greater than the thermal energy generated by non-radiative losses, with each non-radiative recombination contributing a full band gap worth of heat energy. As such, the EQE of the semiconductor must approach unity for

* Part of this chapter, including all figures and tables, is reprinted with permission from “Optically Cooling Cesium Lead Tribromide Nanocrystals” by Benjamin J. Roman, Noel Mireles Villegas, Kylie Lytle, and Matthew Sheldon, 2020. Nano Letters, DOI: 10.1021/acs.nanolett.0c03910. Copyright 2020 by the American Chemical Society.

optical cooling to occur. Despite having internal quantum efficiencies (IQE) exceeding 99%, high quality bulk semiconductors still have to contend with insufficient photon extraction efficiencies due to total internal reflection and parasitic absorption from their surface passivation, losses that are largely an intrinsic feature of the macroscopic semiconductor geometry. [59,92,93]

In recent years, the first instances of measurable laser cooling of semiconductors have been reported by Xiong and coworkers. In their experiments, chemical vapor deposition was used to fabricate semiconductor morphologies that are subwavelength in size in at least one dimension, in order to maximize the optical extraction efficiency of the ASPL, i.e. to promote high EQE via better light management. [49,50] Until our study here, their reports remained the only demonstrations of net optical cooling of a semiconductor, largely due to the difficulty of consistently and reproducibly fabricating materials with sufficiently high EQE.

High quality colloidal semiconducting nanocrystals appear to ubiquitously show ASPL [48] and can be synthesized in subwavelength sizes with EQE above the requisite threshold for net cooling. [94] Notably, recent works have identified all-inorganic cesium lead trihalide perovskite nanocrystals as a material with potential applications for optical cooling due to their near-unity EQE after appropriate surface treatment, making them ideal candidates for demonstrating optical cooling, see also Chapter 3. [53,57,84,95]

Here, I report for the first time the optically driven cooling of colloiddally prepared semiconducting nanocrystals—specifically CsPbBr₃ nanoparticles. I use the

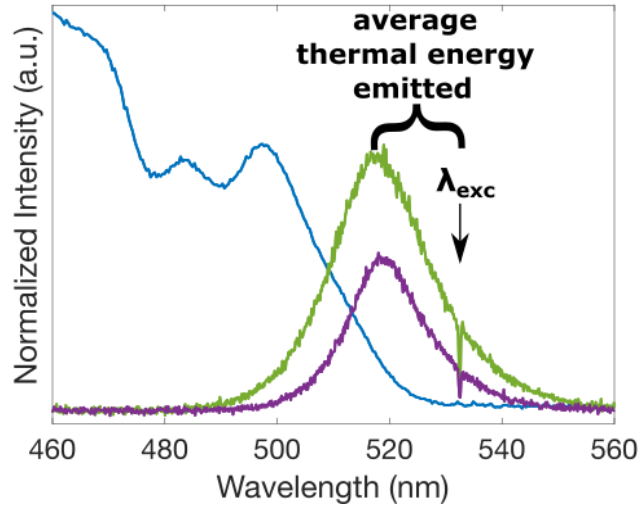


Figure 4.1: CsPbBr₃ absorbance (blue) and anti-Stokes photoluminescence when the nanocrystals are at 25 °C (purple) and 65 °C (green).

known Arrhenius behavior of the ASPL yield to estimate the change in temperature of the nanocrystals during below gap excitation. The rate of cooling, as well as the final temperature reached, are shown to be dependent on the excitation laser fluence.

Additionally, I verify the temperature change of the environment around the nanocrystals by monitoring the anti-Stokes to Stokes Raman scattering ratio of a silicon substrate on which CsPbBr₃ nanoparticles were deposited. This analytical thermometry technique measures the temperature-dependent phonon mode population of silicon to report the local temperature of the substrate.

The necessary EQE threshold for cooling can be calculated by considering the amount of thermal energy emitted with each photon, as defined by the anti-Stokes shift between the excitation wavelength and the emission wavelength. [45] In this study, 532 nm excitation of CsPbBr₃ produces PL centered between 513 to 517 nm depending on

the sample (Figure 4.1). This corresponds to an anti-Stokes shift of approximately 70 to 90 meV. This has previously been established as a one photon up-conversion process whereby absorption of multiple phonons converts below-bandgap absorption into band edge emission. [53,54,57,84] Thus, for every photon emitted, approximately 70 to 90 meV of thermal energy is removed from the semiconductor. In contrast, every instance of non-radiative recombination adds 2.4 eV of thermal energy into this system. For ASPL to remove more thermal energy than the thermal energy added through non-radiative recombination, ASPL emission into free space must occur with greater than ~97% efficiency.

4.2. Methods

4.2.1. Synthesis of CsPbBr₃ Nanoparticles

The synthesis of CsPbBr₃ is based on the method first reported by Protesescu et al. [1] The NH₄SCN treatment is based on the method first reported by Koscher et al. [21]

4.2.1.1. Synthesis of CsPbBr₃ Nanoparticles

Cs₂CO₃ (0.200 g), OA (0.624 mL), and ODE (10 mL) were added to a 25-mL 3-neck round bottomed flask and heated for 1 hour at 120°C under vacuum to dry. After 1 hour, the flask was put under argon and heated to 150°C until all the Cs₂CO₃ had reacted. PbBr₂ (0.069 g) and ODE (5 mL) were added to a 25-mL 3-neck round bottomed flask and heated under vacuum to 120 °C for 1 hour. The solution was then placed under argon, and dried OAm (0.5 mL) and dried OA (0.5 mL) were injected to solubilize the PbBr₂. The temperature increased to 180°C, and the Cs-oleate (0.4 mL)

was swiftly injected. After 1 minute, the solution was cooled with an ice bath. The final solution was centrifuged at 3000 g-forces for 5 minutes and the supernatant was discarded. The precipitate was dispersed in hexane.

4.2.1.2. NH₄SCN Surface Treatment

NH₄SCN was added to a vial of CsPbBr₃ suspended in hexane and vigorously stirred for between 20 and 30 minutes. The resulting cloudy solution was centrifuged at 3000 g-forces for 5 minutes, and the supernatant was decanted and analyzed.

4.2.2. Characterization Methods

4.2.2.1. Determination of Sample EQE

Sample EQE was determined versus a standard solution of fluorescein in 0.1 M NaOH. The absorbance of a dilute solution was collected on an Ocean Optics Flame-S-UV-Vis spectrometer with an Ocean Optics DH-200-Bal deuterium and halogen lamp light source. Photoluminescence was collected on the same Ocean Optics Flame-S-UV-Vis spectrometer, using a Fianium WhiteLase supercontinuum laser ported through an LLTF high contrast filter as the excitation source.

4.2.2.2. Calibration of ASPL Energy of Activation

100 μ L of NH₄SCN treated CsPbBr₃ was diluted with 1 mL of hexane. Several drops were sandwiched between two glass slides and sealed inside of a plastic bag in an argon filled glove box. The sample was clamped in place in an ice bath at a 45 degree angle to the 532 nm CW laser excitation source. Two Edmund Optics OD4 532 nm notch filters were used to block scattered light from the laser. A Stanford SR830 lock-in connected to a Thor Labs DET100A2 detector was used to collect the sample ASPL. The

temperature of the sample was measured with a Digi-sense TC9000 advanced temperature controller and a temperature probe in the ice bath. The ice bath was stirred with a magnetic stir bar to ensure uniformity in temperature. Once the ice in the ice bath had melted, the ASPL was periodically measured as the water bath and sample warmed up to room temperature. The laser was blocked in between measurements.

4.2.2.3. Measurement of Below-gap Excitation Photoluminescence (ASPL)

ASPL was measured using a 532 nm Nd:YAG CW laser ported through a WITec alpha 300 RA confocal microscope, focused on the sample using a long working distance 20x objective with a 0.35 numerical aperture. Between 5 and 100 μL of NH_4SCN treated CsPbBr_3 was added to 1 mL of a 5% by w.t. solution of polystyrene in toluene. One drop was placed on a quartz slide and allowed to dry. The sample was then placed in a Linkam Instruments TS1500 thermal stage attached to the WITec alpha 300 RA confocal microscope. Measurements were taken at a vacuum pressure 0.010 mBar.

4.2.2.4. Measurement of Silicon Raman Scattering

10 μL of NH_4SCN treated CsPbBr_3 was diluted with 500 μL of hexane and dropcast on a clean silicon substrate. The sample was then analyzed as described above for the measurement of below-gap excitation photoluminescence, except with a 20x near working distance objective with a numerical aperture of 0.4.

4.3. Results and Discussion

CsPbBr_3 nanoparticles were synthesized following the hot-injection method established by Protesescu and coworkers. [1] They were then treated with NH_4SCN to increase their EQE to approximately unity. In this reaction, SCN^- removes the excess

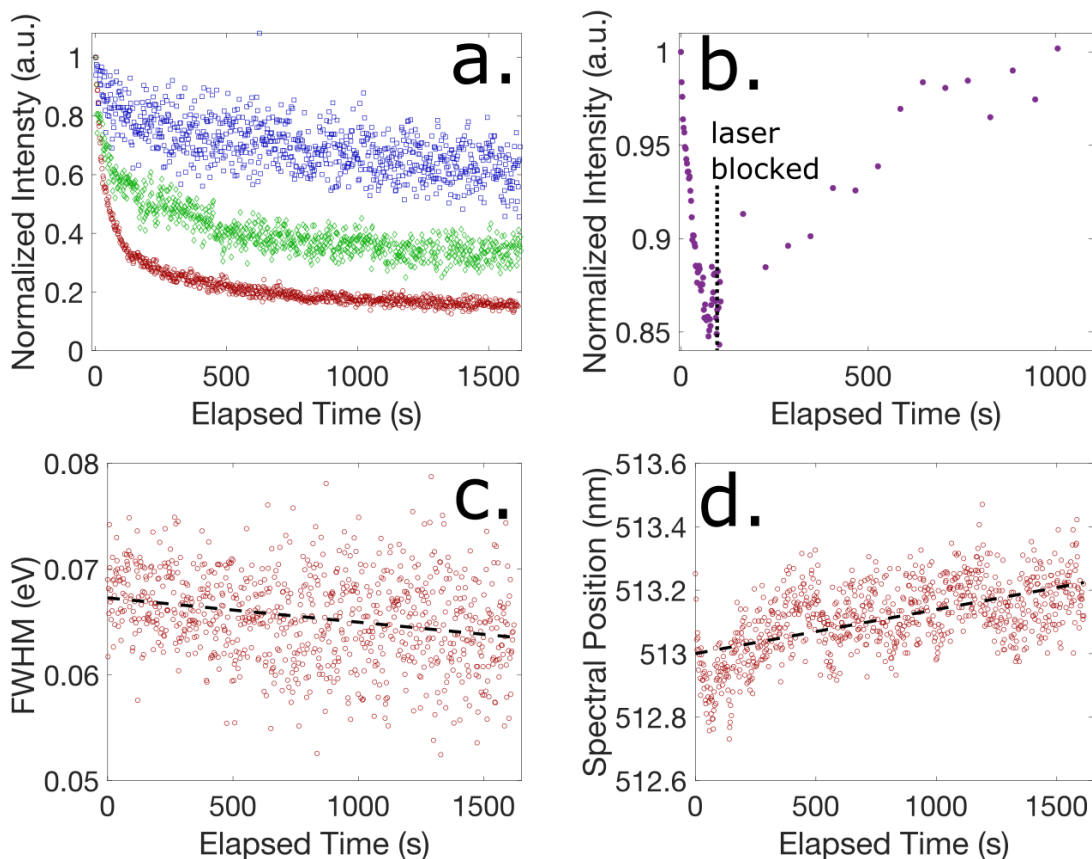


Figure 4.2: CsPbBr₃ anti-Stokes photoluminescence spectral changes during below-gap (532 nm) excitation. (a) Excitation fluence dependent decrease in ASPL intensity over time. Blue squares, green diamonds, and red circles correspond to excitation fluences of 300, 1500, and 3000 W/cm² respectively. (b) CsPbBr₃ pumped below-gap (532 nm) at a fluence for 15 W/cm² for 100 seconds. The laser was then blocked, as indicated by the dotted line. The laser was unblocked periodically to check the ASPL intensity. (c) ASPL decrease in full-width at half-max with an excitation fluence of 3000 W/cm². (d) Red shift of ASPL spectral position with an excitation fluence of 3000 W/cm². In (c) and (d) the dashed line is a linear fit to the data. These data sets are from the same experiment as the red circles in (a).

lead atoms on the nanocrystal surface that are understood to be the predominant source of mid-gap states. [19,21,22] After treatment with NH₄SCN, the sample was confirmed to have $98.5 \pm 4\%$ EQE measured against a fluorescein standard. [96] To demonstrate cooling, these nanoparticles were mixed into a 5% solution of polystyrene in toluene, drop-cast on a quartz slide, and placed under vacuum. Both the polystyrene

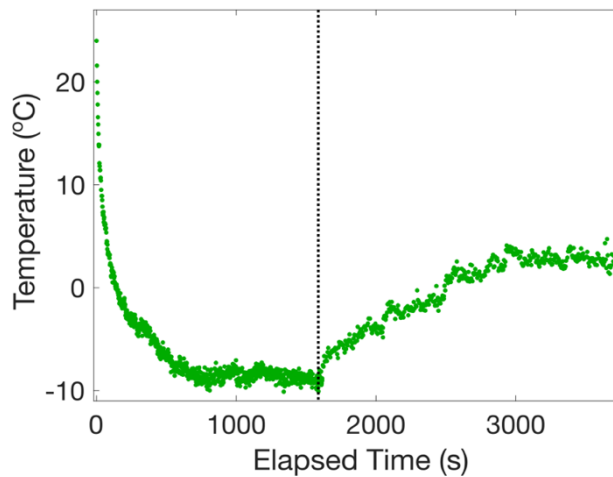


Figure 4.3: NH_4SCN treated CsPbBr_3 excited below gap (532 nm) at a fluence of 4600 W/cm^2 until the temperature reached a steady state. The laser fluence was then decreased to 2300 W/cm^2 until the temperature once again reached a steady state. The dotted line indicated when the laser fluence was decreased. The temperature was estimated using equation 4.1.

encapsulation and the vacuum were used to thermally isolate the nanoparticles, reducing their thermal load to maximize the observed cooling. The sample was then excited using 532 nm CW laser excitation, and the resultant ASPL spectrum was collected continuously or at regular intervals during the course of an experiment.

During below-gap excitation, the collected ASPL spectra changed over time, decreasing in intensity as well as often undergoing a decrease in its full-width at half-max (FWHM), and a red-shift of the spectral position of the photoluminescence (PL) peak (Figure 4.2). Figure 4.2a highlights the decrease in ASPL intensity as a function of the excitation fluence, with greater light intensity leading to a faster rate of decrease. Given enough time, the ASPL stabilized at a saturation point, where it remained steady so long as the excitation fluence was not increased or decreased (Figure 4.3). Most

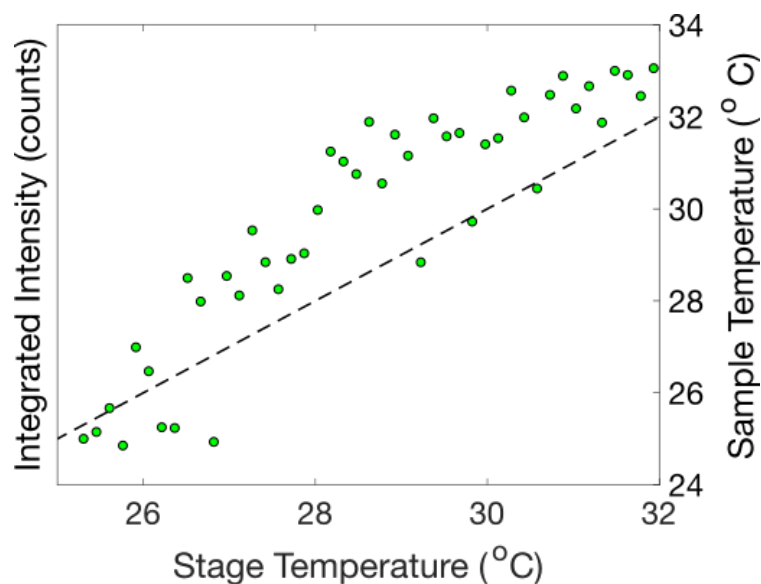


Figure 4.4: The temperature reported by the internal thermocouple of a heating stage plotted versus the temperature (right axis) estimated using the change in CsPbBr₃ ASPL intensity (left axis) according to equation 4.1. The dashed line corresponds to the temperature reported by the thermocouple.

tellingly, this change in the ASPL intensity was entirely reversible, either through blocking the laser (Figure 4.2b) or through decreasing the excitation fluence once the ASPL decay reached its saturation point (Figure 4.3). The reversibility of the change in ASPL intensity is an important characteristic that differentiates the spectral changes observed here from non-reversible photodegradation that has been observed when CsPbBr₃ nanoparticles are exposed to trace water, O₂, or other environmental factors that degrade their electronic structure. [97]

ASPL is a thermally activated process. As such, ASPL yield increases with increasing temperature (Figure 4.1 and 4.4), and conversely decreases with decreasing temperature. Thus, I hypothesize that the observed decrease in the intensity of the ASPL

spectra is due to the thermal deactivation of the nanoparticles brought about by a net decrease in temperature. Additional verification that this decrease in ASPL signal corresponds to a decrease in temperature can be seen in the FWHM of the ASPL spectra (Figure 4.2c). A decrease in the FWHM of the ASPL peak over the course of the measurement is consistent with a decrease in the thermal activation of carriers participating in optical recombination across the semiconductor band gap. Similarly, a red-shift of the ASPL peak position (Figure 4.2d), also indicates thermal de-activation of the energy distribution of carriers recombining across the band gap as temperature is decreased. [58,98–100]

During ASPL, each up-converted emission event can be thought of as a cooling cycle that removes thermal energy by depopulating the phonon modes of the nanoparticle. The depopulation of the phonon modes in turn reduces the ASPL yield and the amount of thermal energy that is removed per unit time, even under a constant laser fluence. This photo-induced thermal deactivation is manifest in the fluence dependence of the rate of the ASPL signal decay we observe: Higher laser fluences remove a greater amount of thermal energy per unit time, causing a faster decay in the ASPL intensity (Figure 4.2a). After significant thermal deactivation, the ASPL yield becomes too low to overcome the thermal energy entering the nanocrystals from their environment, and the ASPL intensity approaches a constant value. This constant ASPL intensity corresponds to a steady state when thermal energy flowing into the nanocrystals from the environment is equal to the thermal energy removed per unit time via ASPL. Critically, the observed reversibility of this decay signal is due to this thermal dependence of the

ASPL mechanism. When the ASPL is no longer being pumped (i.e. the laser is blocked) or the rate of heat removal via ASPL is decreased such that it no longer counterbalances the thermal energy from the nanoparticles' environment (i.e. the laser fluence is decreased), the nanoparticles increase in temperature and the ASPL intensity increases as a consequence. In the former case, when the laser is blocked, the nanoparticles will warm back up to room temperature, as demonstrated in Figure 4.2b. In the latter case, when the laser fluence is decreased, the ASPL intensity increases until the nanoparticles once more reach a steady state, and the ASPL intensity remains constant (Figure 4.3) with the nanocrystals at a temperature once again dictated by the rate balance of heat removal due to ASPL and heat provided from their environment.

The temperature dependence of the ASPL intensity from CsPbBr₃ nanocrystals is known to follow an Arrhenius relation, with the natural log of the intensity directly proportional to 1/T, as discussed in Chapter 3. [57] Thus, the change in temperature required to bring about a given change in ASPL intensity can be estimated using equation 4.1, which is simply the ratio of two Arrhenius equations solved for some unknown temperature:

$$T = \left[\frac{k_B}{E_a} \ln \left(\frac{I_0}{I} \right) + \frac{1}{T_0} \right]^{-1} \quad (4.1)$$

In this, I_0 is the integrated ASPL intensity at some known temperature, T_0 ; I is the integrated ASPL intensity at some new temperature, T ; k_B is Boltzmann's constant, and E_a is the energy of activation of the one photon up-conversion process. In Chapter 3, the

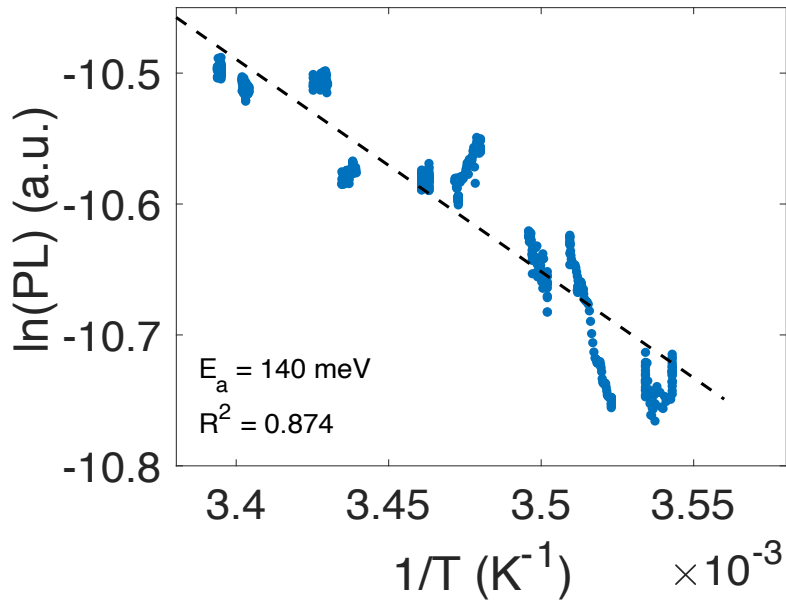


Figure 4.5: An Arrhenius plot of the temperature dependence of NH_4SCN treated CsPbBr_3 ASPL over the temperature range 10–24 °C. The estimated energy of activation was 140 meV.

ASPL energy of activation for CsPbBr_3 was estimated by heating the nanocrystals in a thermal stage. [57] Alternatively, for this study a thin film sample of nanocrystals was cooled using an ice water bath in order to ensure that the estimated energy of activation was comparable for the temperature range over which optical cooling was observed. The energy of activation was estimated to be ~ 140 meV (Figure 4.5), in line with previously published measurements. [57,58]

As a check of equation 4.1, a sample of CsPbBr_3 nanocrystals was heated on a temperature-controlled heating stage while simultaneously collecting ASPL spectra. The CsPbBr_3 nanocrystals were not treated with NH_4SCN to ensure that the nanoparticles' EQE was below the threshold for optical cooling. The temperature of the nanoparticles,

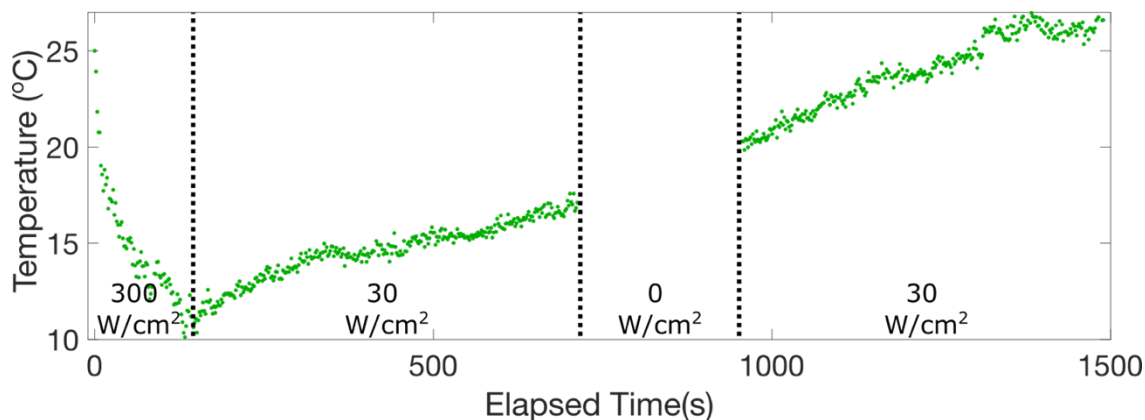


Figure 4.6: Monitoring the temperature of CsPbBr₃ nanocrystals during below-gap excitation (532 nm). The nanoparticles were cooled at an excitation fluence of 300 W/cm², followed by a decreased fluence of 30 W/cm², the laser being blocked, and then 30 W/cm² again.

estimated using equation 4.1, was within a few degrees of the temperature reported by the thermal stage's internal thermocouple, a difference that may be due to local variations in the sample temperature (Figure 4.4). This confirms that equation 4.1 can accurately estimate the temperature of the nanoparticles, at least over the temperature range for which the ASPL energy of activation has been calibrated (10 °C to 25 °C).

For the purposes of estimating the temperature of the nanocrystals during below-gap excitation, the first recorded spectrum for a given spot on the sample is assumed to be approximately room temperature. A decrease—or increase—in ASPL intensity can then be correlated to a change in temperature according to equation 4.1. Figure 4.6 demonstrates a typical cooling experiment. The sample was pumped below-gap with a fluence of 300 W/cm² such that thermal energy was removed faster than it was replaced by the environment surrounding the nanocrystals in the optical spot. The temperature began to drop exponentially, reaching an estimated temperature of ~10 °C after

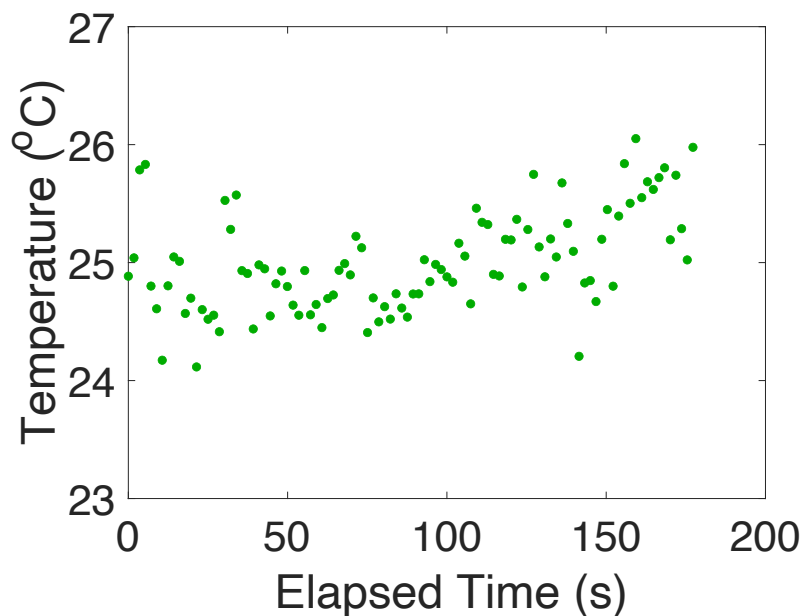


Figure 4.7: NH_4SCN treated CsPbBr_3 nanocrystals, pumped below gap (532 nm) at a fluence of 30 W/cm^2 . The steady ASPL intensity, and thus the temperature estimated using equation 4.1, indicates that this fluence is too low to overcome heat flux from the nanoparticles' environment. This is the same sample analyzed in Figure 4.6.

approximately 2 minutes. This temperature is well within the temperature range over which we calibrated the ASPL energy of activation. The excitation fluence was then decreased to 30 W/cm^2 , below the fluence threshold necessary to overcome the heat flux from the environment into the nanocrystals at this particular spot on the sample, as is shown in Figure 4.7. Therefore, the temperature of the nanoparticles began to increase. The laser was additionally blocked for 5 minutes to demonstrate the continued reversal of the decay in ASPL intensity, even in the dark. After approximately 20 minutes, the nanoparticles returned to room temperature. Figures 4.2a and 4.2b are similarly

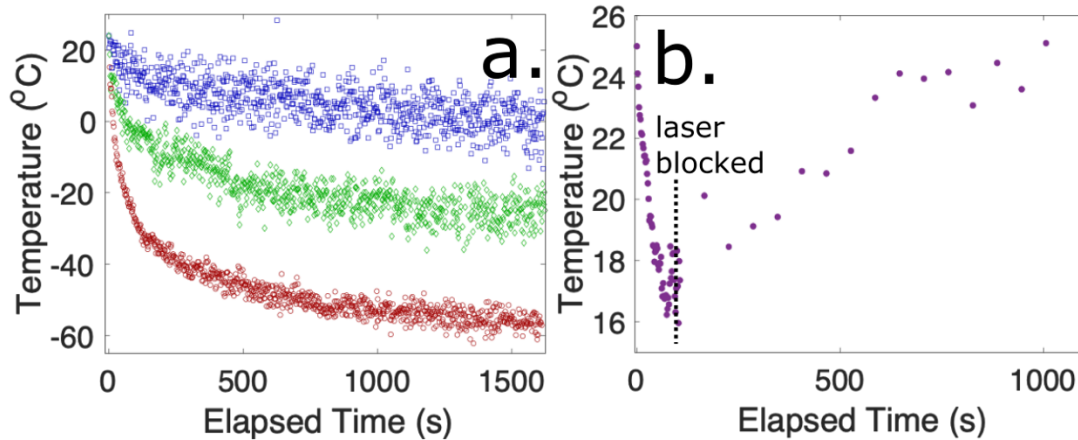


Figure 4.8: CsPbBr₃ anti-Stokes photoluminescence spectral changes during below-gap (532 nm) excitation. (a) Excitation fluence dependent decrease in temperature over time. Blue squares, green diamonds, and red circles correspond to excitation fluences of 300, 1500, and 3000 W/cm² respectively. This data set is the same as in Figure 4.2a, using equation 4.1 to estimate temperature. Note that the temperatures estimated here are only accurate so long as the ASPL energy of activation holds constant over this temperature range. (b) CsPbBr₃ pumped below-gap (532 nm) at a fluence for 15 W/cm² for 100 seconds. The laser was then blocked. The laser was unblocked periodically to check the ASPL intensity. This is the same data set as in Figure 4.2b, using equation 4.1 to estimate temperature.

reproduced as nanoparticle temperature versus time in Figure 4.8a and 4.8b, respectively.

The red-shift, decrease in FWHM, and reversible decrease in intensity of ASPL spectra all strongly suggest that the nanoparticles are experiencing a net decrease in temperature. For additional verification of this hypothesis, we also sought evidence that the nanoparticles were cooling their local environment during ASPL. For this, we took advantage of the well known temperature dependence of Raman scattering from a Si substrate the nanoparticles were deposited on. Silicon has a strong Raman scattering peak at 520 cm⁻². The ratio of the anti-Stokes and Stokes Raman peaks corresponding to

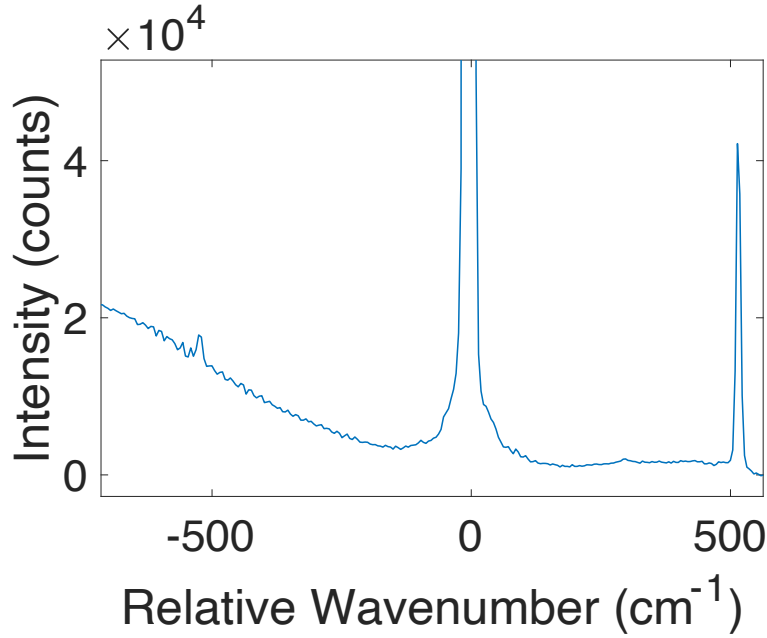


Figure 4.9: Silicon Raman scattering resolved simultaneously to CsPbBr₃ ASPL.

this vibrational mode can be used to determine the absolute temperature of the silicon, as described in equation 4.2, where I_{AS} and I_S are respectively the silicon anti-Stokes and Stokes scattering intensities, ν_l and ν_v are respectively the frequencies of the laser and the silicon vibrational mode, h is Planck's constant, k_B is Boltzmann's constant, and T is the temperature of the silicon. [101]

$$\frac{I_{AS}}{I_S} = \left(\frac{\nu_l + \nu_v}{\nu_l - \nu_v}\right)^3 e^{\frac{-h\nu_v}{k_B T}} \quad (4.2)$$

As the temperature of the silicon decreases, the phonon mode corresponding to ν_v is depopulated, and the anti-Stokes scattering peak decreases in intensity relative to the Stokes scattering peak. It is important to note that equation 4.2 does not require prior calibration, as it directly correlates the temperature dependence of the ν_v phonon mode

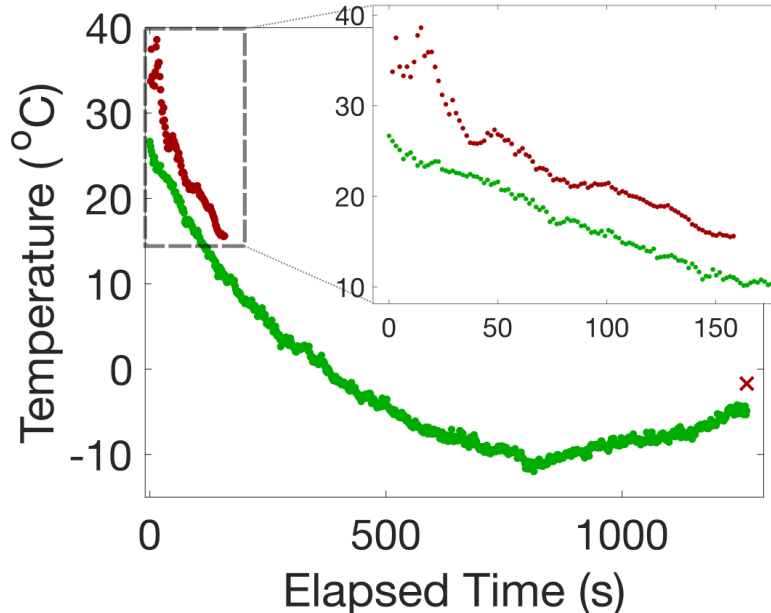


Figure 4.10: Temperature of CsPbBr₃ nanoparticles during below gap excitation, estimated using the CsPbBr₃ ASPL intensity (green) as well as the anti-Stokes to Stokes Raman scattering ratio of Si (red). At the end of the measurement, the focus was adjusted to maximize the silicon Raman scattering collection efficiency. The final temperature of the silicon substrate is reported as the red x.

population with the ratio of the accompanying Stokes and anti-Stokes scattering cross sections.

To confirm that the nanoparticles were indeed decreasing the local temperature, NH₄SCN treated CsPbBr₃ nanoparticles were dropcast onto a cleaned silicon wafer and placed under vacuum. The nanoparticles were excited at a focal plane just above the substrate surface that maximized ASPL intensity, so as to maximize the thermal energy removed per unit time. The silicon Raman signal could be resolved simultaneously to the ASPL intensity (Figure 4.9). The temperature estimated by the change in ASPL according to equation 4.1 is plotted in Figure 4.10 alongside the temperature determined

by the silicon anti-Stokes to Stokes ratio according to equation 4.2. Note that after 160 seconds, the anti-Stokes silicon peak was too low in intensity to be resolved against the noise. After ~800 seconds, the CsPbBr₃ ASPL intensity began to increase again, possibly indicating that the nanoparticles were being damaged under the high fluence necessary to resolve the silicon Raman peaks (10^5 W/cm²) and were beginning to heat. At the end of the measurement, the focal plane was optimized so that the silicon Raman signal could once more be resolved with a good signal-to-noise ratio in order to measure the final temperature of the silicon substrate.

The temperature reported by the silicon Raman scattering is remarkably close to the temperature estimated using the CsPbBr₃ ASPL, with the silicon just a few degrees higher than the nanoparticles themselves. The temperature of the silicon at this final time was determined to be -1.7 °C, as compared to the final temperature of the nanoparticles, estimated to be -5 °C. Note that the change in the temperature of the silicon is certainly a locally induced change in the vicinity of the optical spot. Further study and optimization will be necessary to use CsPbBr₃ nanoparticles to induce a net decrease in temperature for a bulk thermal load.

4.4. Conclusions

In conclusion, I analyzed both the temperature dependent yield of ASPL and the anti-Stokes to Stokes Raman scattering ratio of a silicon substrate to confirm that below gap excitation of CsPbBr₃ nanoparticles can induce a net decrease in temperature. A remarkable aspect of these experiments is the reproducibility and consistency with which CsPbBr₃ nanoparticles can be optically cooled. While the rate and magnitude of the

cooling are dependent on the local environment and thermal insulation of each spot analyzed in our experiments, nearly every measurement showed an exponential and reversible decrease in nanoparticle temperature. It is currently unclear whether the ease with which CsPbBr₃ nanoparticles exhibit optical cooling is a result of their unique photophysical characteristics, or whether cooling should be expected as a general feature of ASPL with near-unity EQE. Certainly, the observed cooling is comparable in magnitude and timescale to that reported by Xiong and co-workers. [49,50] The comparison between studies suggests that the optical cooling may, in fact, be a feature of the high EQE, and the optical extraction efficiency afforded by the sub-wavelength geometry. As such, colloidal semiconductor nanoparticles with high quantum yield may likely provide an ideal platform for the study and application of optical cooling moving forward.

5. PLASMONIC ENHANCEMENT OF ONE PHOTON UP-CONVERSION*

5.1. Introduction

As discussed in Section 1.1, perovskite nanoparticles demonstrate Stokes shifted PL (SSPL) with quantum efficiencies as high as 100%. [21] Additionally, the cooling demonstrated in Chapter 4 requires that the ASPL EQE be greater than 96%. As discussed in Chapter 3, such a high efficiency seems at odds with the need for mid-gap intermediate states, as all-inorganic perovskite nanoparticles are understood to be generally absent of mid-gap trap states. [19] Indeed, the results in Chapter 3 suggest that mid-gap trap states act as loss pathways rather than necessary intermediate excited states for ASPL. Rather, it is possible that the ASPL excitation mechanism proceeds through a virtual state, in a manner more analogous to anti-Stokes Raman scattering. As such, it may be feasible to increase the thermal scavenging potential of the ASPL using a plasmonically active substrate, leveraging the same light-matter interactions that can also enhance Raman scattering, as is well known for surface enhanced Raman spectroscopy (SERS). [102] The localized surface plasmon resonance of a metal nanostructure, e.g. gold nanoparticles, enhances the optical field and increases the local-mode density of the electromagnetic field, improving the coupling efficiency of the electromagnetic excitation to vibrational modes, i.e. phonons, in the nanocrystal lattice.

* Part of this chapter, including all figures and tables, is reprinted with from “Six-fold plasmonic enhancement of thermal scavenging via CsPbBr₃ anti-Stokes photoluminescence” by Benjamin J. Roman and Matthew T. Sheldon, 2019. *Nanophotonics*, 8, 599–605, Creative Commons 4.0.

Here, I report the modification of CsPbBr₃ ASPL through coupling to Au nanoparticles deposited on a glass substrate. Two regimes of coupling are examined using confocal fluorescence microscopy. When Au nanoparticles are limited to approximately 3 to 4 particles for every diffraction-limited region, called low coverage from hereon, the ASPL blue-shifts by as much as 7.2 meV compared with the ASPL of control samples of pure films of CsPbBr₃ nanoparticles without Au nanoparticles. This blue-shift corresponds to a fraction of the longitudinal optical phonon, which is known to have energy of ~ 20 meV in CsPbBr₃ nanoparticles. When CsPbBr₃ nanoparticles are deposited on a substrate coated in a monolayer film of densely packed Au nanoparticles, called uniform coverage from hereon, the ASPL both blue-shifts and increases in intensity relative to the SSPL measured over the same region. The blue-shift indicates a greater amount of thermal energy scavenged per emitted photon during ASPL and is likely due to a decrease in the fluorescent lifetime. In contrast, the increase in ASPL yield relative to SSPL is due to plasmonic enhancement of the intrinsic ASPL mechanism. These two effects, and the accompanying six-fold improvement in overall thermal energy scavenging, may help enable future optoelectronic applications of optical cooling, and are an intriguing method of improving the ASPL performance in all-inorganic perovskite nanoparticles by coupling them with Au nanoparticle plasmons.

5.2. Methods

5.2.1. Preparation of Samples

5.2.1.1. Synthesis of CsPbBr₃ Nanocrystals

CsPbBr₃ nanoparticles were prepared following the procedure established by Protesescu et al. In short, 0.200 g Cs₂CO₃, 0.624 mL OA, and 10 mL ODE were added to a 25-mL 3-neck flask and heated at 100°C under argon flow until the Cs₂CO₃ had entirely dissolved to form Cs-oleate. In a separate 25-mL 3-neck flask, 0.069 g PbBr₂ and 5 mL ODE were dried at 120°C under vacuum for 1 hour. The solution was then placed under argon, and 0.5 mL of dried OAm and 0.5 mL of dried OA were injected to solubilize the PbBr₂. The temperature was increased to 180°C, and 0.4 mL of the Cs-oleate solution was swiftly injected. After 3 seconds, the solution was cooled with an ice bath. The final crude solution was centrifuged at 3000 g-forces for 5 minutes, and the supernatant was discarded. The precipitate was cleaned three times using a combination of ODE and hexane

5.2.1.2. Preparation of Films

Quartz substrates were initially cleaned by sonicating in methanol for 1 hour. The substrates with gold were placed in a vial with 1.5 mL nanopore water, 60 µL of 0.1 M HCl, and an amount of the aqueous gold nanoparticles, and then the vial was centrifuged for 1 hour at 3000 g-forces. The substrate was then rinsed with hexane before depositing perovskites. To each substrate, 1 µL of the stock CsPbBr₃ solution was drop-cast, allowed to dry, and then another 1 µL was added. All optical measurements were taken

through the cover slip to ensure that regions of CsPbBr₃ coupled to gold nanoparticles were being probed.

5.2.2. Characterization Methods

5.2.2.1. Initial Nanoparticle Characterization

Initial characterization included UV-Vis and PL, as well as transmission electron microscopy (TEM), and are available in the SI. UV-Vis spectra from 300-800 nm were collected on an Ocean Optics Flame-S-UV-Vis spectrometer with an Ocean Optics DH-200-Bal deuterium and halogen light source. TEM images were collected on an FEI Tecnai G2 F20 ST FETEM microscope, operating at 200kV. The CsPbBr₃ nanoparticles are cuboids with edge lengths of 10.27 ± 0.18 nm, as determined by analyzing 60 particles.

5.2.2.2. Analysis of ASPL

All measurements of up-conversion were taken using a WITec alpha 300 RA confocal microscope with an EC Epiplan-NEOFLUAR 100x objective with a 0.9 numeric aperture. Measurements were taken at room temperature as a series of spectra, using a piezoelectric stage to raster scan an area of the sample. Each measurement was taken over a 10 μ m by 10 μ m area as a series of 35 lines of 35 spectra. ASPL was measured using a 532 nm Nd:YAG CW laser. SSPL was measured using a 405 nm diode CW laser. ASPL spectra were collected with an excitation fluence of 2000 W/cm². SSPL spectra were collected with an excitation fluence of 1000 W/cm². The power dependence of the ASPL was determined using a range of laser fluences from 2000 to 50000 W/cm².

Each spectrum was processed using WITec's Project FOUR software to remove cosmic rays before further analysis.

5.2.2.3. Simulation of Au Nanoparticle Field Enhancement

The simulation was run using a commercially available FDTD solver (Lumerical). A 40 nm diameter gold nanoparticle with refractive index as measured by Johnson and Christy [103] was simulated in a medium with refractive index of 2.25 as an approximation of the CsPbBr₃ nanoparticles surrounding the Au nanoparticles [104]. The gold nanoparticle was illuminated with a plane wave source at 532 nm in a simulation area using PML boundary conditions.

5.2.2.4. Measurement of SSPL Lifetime

Fluorescence lifetime was measured using an Olympus FV 1000 confocal platform with a PicoQuant TCSPC FLIM add-on. Samples were excited using a 405 nm pulsed laser. Data was fit to a biexponential decay using Olympus Life Science's proprietary Fluoview FV1000 software suite.

5.3. Results and Discussion

In order to elucidate the interactions between CsPbBr₃ and gold nanoparticles, two substrates were prepared with varying amounts of 40 nm diameter gold nanoparticles deposited onto coverslips *via* centrifugation: one with 50 Au nanoparticles per μm^2 corresponding to approximately 3 to 4 gold nanoparticle per diffraction limited region, and one with 250 Au nanoparticles per μm^2 corresponding to a monolayer of Au nanoparticles. A clean glass cover slip was used as the control substrate. CsPbBr₃

nanoparticles were drop-cast onto these substrates by depositing a 1 μL drop of the stock solution, letting it dry, and then adding a second 1 μL drop. Optical measurements were taken through the back of the coverslip to ensure that regions coupled to gold nanoparticles were directly probed.

Table 5.1: Average position, full width at half max, and average thermal energy scavenged by each up-converted photon.

	SSPL Position (nm)	ASPL Position (nm)	SSPL FWHM (meV)	ASPL FWHM (meV)	Scavenged Energy (meV)
Control Sample	512.88 ± 1.00	514.39 ± 0.82	63.3 ± 5.0	72.8 ± 1.4	79.8
Low Au Coverage	512.38 ± 2.62	512.86 ± 0.45	56.5 ± 9.8	70.96 ± 2.7	87.0
Uniform Au Coverage	512.63 ± 3.33	512.24 ± 2.72	47.4 ± 16.1	70.5 ± 4.9	89.9

A confocal microscope with a 100x objective was used to raster scan 10 μm by 10 μm regions of the samples. The same region was scanned first with a 405 nm CW laser to measure SSPL, then with a 532 nm CW laser to probe ASPL. 1225 individual spectra were taken during each scan. Each spectrum was then used as a data point for further statistical analysis. The major findings are summarized in Table 5.1.

From the control sample, it can be seen that the ASPL is red-shifted and broadened in comparison with the SSPL taken over the same region (Table 5.1). This red-shift has been observed before and has been previously attributed to an ensemble

effect, as single particle measurements show identical ASPL and SSPL. [84] In this case, there may be energy transfer between closely spaced particles, with emission occurring from the lowest-energy emitting state available in a region. With low Au nanoparticle coverage, two major changes in the ASPL behavior are identified. First, the average FWHM of both the SSPL and ASPL decreases. Second, the ASPL blue-shifts by an average of 7.2 meV in comparison with the control sample. This blue-shift is significant because it indicates that each emitted photon scavenges more thermal energy. With uniform Au nanoparticle coverage, the trend in average ASPL position and FWHM continues monotonically with a decrease in the FWHM and a further blue-shift of the ASPL spectral position. In comparison with the control, the uniform Au nanoparticle coverage sample emits an additional 10.1 meV of thermal energy per up-converted photon. It is known that coupling fluorescent semiconductors to a metal decreases their fluorescent lifetime, [105] and this has been additionally demonstrated for CsPbBr₃ with Au nanoparticles deposited on the perovskite surface, as discussed in Chapter 2. [43] One explanation of the blue-shift reported here may be that the reduction in the fluorescence lifetime prevents the energy transfer between particles that would result in red-shifted emission. In fact, I observed a monotonic decrease in the SSPL lifetime of the CsPbBr₃ nanoparticles with increasing Au coverage, from 3.15 ns in the control sample, to 2.44 ns with low Au coverage, and finally 2.25 ns with uniform Au coverage.

Notably, the standard deviation in both ASPL peak position and FWHM increases in the sample with uniform Au nanoparticle coverage. This trend highlights the

major difference between the two Au nanoparticle coverage regimes. At low Au nanoparticle coverage, the majority of Au nanoparticles in a region are more than 10 nm away from other gold nanoparticle and near-field optical coupling dominates the Au-perovskite interactions. The resulting decrease in fluorescent lifetime results in excitation and emission from the same perovskite particle, before energy transfer between perovskite particles takes place. With uniform densely packed Au nanoparticle coverage, very short-range optical hot spots (smaller than a few nanometers) are expected to play a more significant role, leading to the stochastic modification of the ASPL emission that is dependent on the local order of the Au nanoparticle film, as well as the large increase in the standard deviation of the SSPL position and FWHM. While the ASPL position is nearly identical to the SSPL position in the sample with uniform Au coverage, the ASPL FWHM is much larger than that of the SSPL over the same region of the sample. This suggests that the phonon mediated up-conversion may emit from a different distribution of states than those accessible through above band gap excitation.

It is interesting to note that the longitudinal optical (LO) phonon of CsPbBr₃ has an energy of approximately 20 meV, [85] which is less than the thermal energy emitted per photon, even in the control sample. As such, each up-converted photon is scavenging the thermal energy of multiple phonons. This is especially remarkable when compared to other semiconductor materials studied for optical cooling applications which have larger LO phonon energies, but only emit a single phonon worth of thermal energy with every

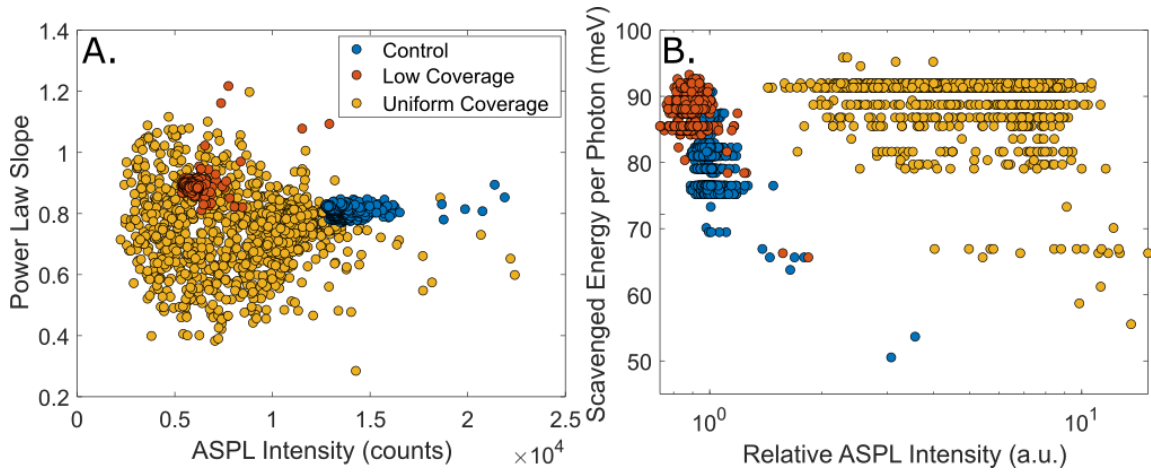


Figure 5.1: (A) ASPL intensity versus the power law slope of the ASPL excitation power dependence. (B) ASPL Intensity normalized to the SSPL intensity in the same region plotted against the average scavenged thermal energy per photon emitted. The relative ASPL intensity is scaled so that a value of 1 corresponds to the average value for the control.

up-converted photon. [106] The 10 meV blue shift of the ASPL demonstrated with uniform Au coverage represents an additional half phonon of thermal energy extracted per photon.

Using the relationship $PL \propto I^b$, where PL is the ASPL intensity and I is the excitation power density, a log-log plot of laser fluence versus integrated ASPL counts may be used to extract b , which gives information about the excitation process. For an ideal one photon process, every absorbed photon produces an emitted photon, and b is expected to be 1. However, a number of interactions, such as particle charging, may lead to b with a value less than 1. As with FWHM and ASPL spectral position, the standard deviation of this power law slope increases dramatically with uniform Au nanoparticle

coverage, as shown in Figure 5.1a which plots ASPL integrated counts versus power law slope as a scatter plot, with each point corresponding to a diffraction limited region on the sample. This spread in the power dependence of the ASPL intensity is not present with low Au nanoparticle coverage, suggesting stochastic short-range interactions with the Au nanoparticles are modifying the intrinsic ASPL mechanism.

As is additionally demonstrated in Figure 5.1a, the raw counts of ASPL are decreased to approximately 1/3 of the control value for the sample with low Au nanoparticle coverage. The average ASPL counts are further decreased in the sample with uniform coverage, however the standard deviation is greatly increased. It is important to note that plasmonic substrates are known to quench PL from semiconductors that are within 4 to 5 nm of the metal surface, so this decrease in ASPL is not unexpected. [107] If, however, the ASPL counts are normalized to the SSPL counts from the same region, a different trend emerges. When normalized to SSPL intensity, the relative ASPL is observed to decrease with low Au nanoparticle coverage, but increase with uniform coverage, as shown in Figure 5.1b. Here, the relative ASPL intensity is the integrated ASPL counts divided by the integrated SSPL counts for each region and normalized so that the value 1 is equal to the average intensity of the control. The scavenged energy per photon is the thermal energy required to up-convert a photon with 2.33 eV of energy (532 nm excitation source) to the spectral center of the ASPL. This plot clearly demonstrates the average blue-shift of the ASPL with increasing amounts of Au, as well as the increase in ASPL relative to its respective SSPL.

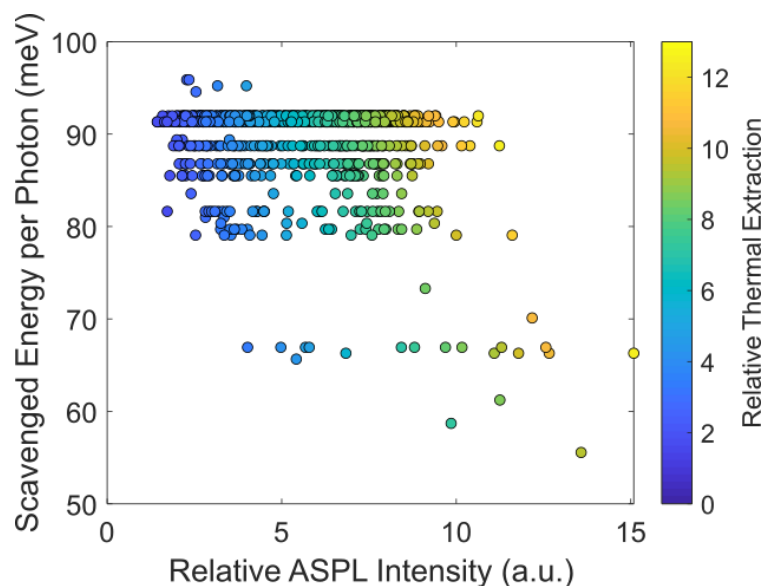


Figure 5.2: Relative ASPL intensity versus scavenged thermal energy per emitted photon for the sample with uniform Au nanoparticle coverage. The color of each point corresponds to the scavenged thermal energy per photon multiplied by the relative ASPL intensity and normalized to the average corresponding value for the control.

In order to estimate the plasmonic enhancement of ASPL thermal scavenging for each sample, I multiplied the relative ASPL intensity, as shown in Figure 5.1b, by the scavenged energy per photon. Essentially, this approximates each count as a single emitted photon with energy equal to the ASPL spectral center. An example of this is shown visually in Figure 5.2, where the color indicates the thermal energy scavenged at each point relative to the thermal energy scavenged, on average, by the control sample. The samples with Au nanoparticles scavenge 6.72 and 0.97 times the thermal energy that the control sample scavenges, for the high and low Au nanoparticle coverage samples, respectively. While the high coverage sample shows an impressive enhancement of

thermal scavenging, the low coverage sample shows the utility of the blue-shifted ASPL. The 7.2 meV blue-shift almost entirely makes up for the 15% decrease in relative ASPL intensity. It is important to note that these samples are not optimized for integration into a cooling device. The absolute amount of SSPL and ASPL observed decreases with increasing Au coverage due to the photoluminescent quenching that is expected to occur when a semiconductor is in close proximity to a metal nanostructure, as well as the Au nanoparticles acting as scattering centers and promoting reabsorption losses. However, these effects should contribute similarly to the decrease in both ASPL and SSPL. As such, by normalizing ASPL to the SSPL measured over the same region, the quenching effects should be removed from the final estimate of thermal scavenging.

To verify that this 6.7-fold enhancement is in line with what could be expected given the Au nanoparticles' plasmon, a full-wave optical simulation was performed (FDTD method) of a 40 nm in diameter Au nanoparticle embedded in a medium with a refractive index of 2.25, i.e. the refractive index of the CsPbBr₃ nanoparticles. [104] When illuminated with a 532 nm plane wave, the Au nanoparticle shows a 6.5 times field enhancement near its outer surface (Figure 5.3). While the entirety of the improvement of thermal scavenging cannot be attributed to this effect, this simulation does show that the change in thermal scavenging potential reported here is not

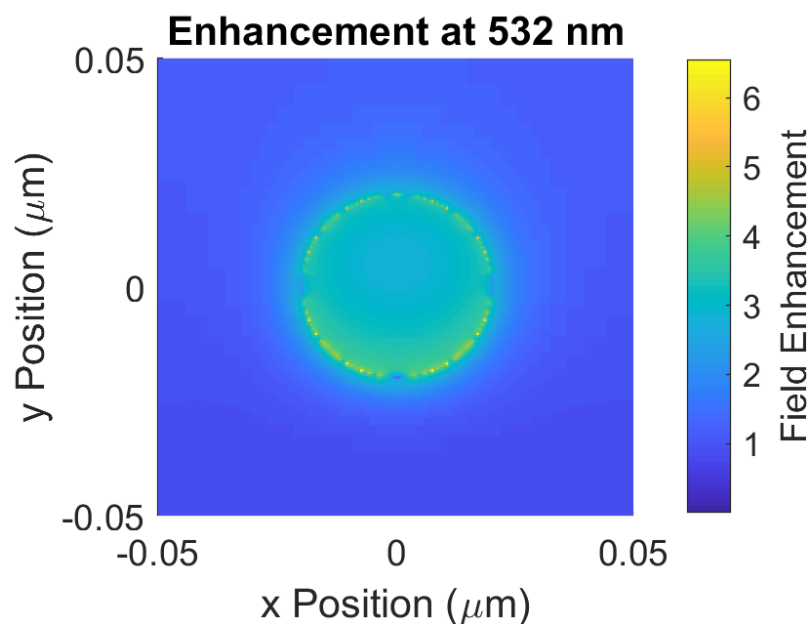


Figure 5.3: Field enhancement of a 40 nm gold nanoparticle surrounded by a material with a refractive index of 2.25.

unreasonable given the field enhancement produced by the gold nanoparticles under these conditions.

5.4. Conclusions

In conclusion, I have discussed the enhancement of CsPbBr₃ nanoparticle ASPL through coupling to a substrate with varying amounts of plasmonically active Au nanoparticles. This enhancement is due to two major effects: a blue-shift in the ASPL spectral center, and an increase in the ASPL intensity relative to the SSPL intensity of the sample. The former phenomenon is likely attributable to a decrease in the fluorescent lifetime when a nanoparticle is coupled to a plasmonically active substrate. The latter

phenomenon, however, is only present with high Au nanoparticle coverage of the substrate and may be analogous to the order of magnitude increase of Raman scattering demonstrated in SERS. Both effects together lead to a 6.7-fold increase in relative thermal extraction by the sample with the highest Au nanoparticle coverage. This enhancement is especially promising for applications in optoelectronic devices, where the fluorescent quenching of the CsPbBr₃ nanoparticles may be managed with more sophisticated photonic design, while still maintaining the enhancement of the ASPL thermal scavenging.

6. CONCLUSIONS

CsPbBr_3 perovskite nanocrystals are a remarkable material with PLQY approaching unity due, in part, to their tolerance to forming mid-gap defect states. Their highly efficient PL makes them a potential target for luminescence up-conversion, where low energy absorbed photons are converted into higher energy emitted photons.

Chapter 2 describes the deposition of gold metal nanocrystals onto the surface of CsPbBr_3 , as well as the competing cation exchange reaction. I demonstrate when AuBr_3 is added to a solution of CsPbBr_3 , pairs of Au(III) and Au(I) exchange with Pb(II) ions from the nanocrystal lattice, generating $\text{Cs}_2\text{Au}_2\text{Br}_6$, a near IR semiconductor. If PbBr_2 is added simultaneously to AuBr_3 , the cation exchange reaction is prevented and gold metal nanocrystals deposit on the surface of the CsPbBr_3 . Typically, metal deposition quenches semiconductor fluorescence. Remarkably, though, Au- CsPbBr_3 heterostructures have PLQY as high as 73%. This high PLQY is important if they are to be utilized for optical applications requiring photoluminescence, such as hot-electron luminescence up-conversion.

Chapter 3 discusses the role of mid-gap defect electronic state in the one photon up-conversion of CsPbBr_3 nanocrystals. It is commonly believed that mid-gap electronic defect states play a role as an intermediate state for nanocrystal ASPL. CsPbBr_3 nanocrystals, however, are not known to form mid-gap states, a quality that is partly responsible for their highly efficient PL. Despite this lack of mid-gap states, CsPbBr_3 show efficient ASPL. In this chapter, I examine the role of mid-gap states in CsPbBr_3

ASPL through studying CsPbBr₃ nanoparticles before and after NH₄SCN treatment—a surface treatment reaction that increases the CsPbBr₃ PLQY to unity, essentially removing all mid-gap states. I show that when all mid-gap states are removed, the ASPL efficiency increases, suggesting that these mid-gap states act as loss pathways and are not necessary for efficient ASPL. Additionally, I use the thermal dependence of the ASPL to demonstrate that the energetics of CsPbBr₃ ASPL is not significantly changed when the mid-gap states are removed, suggesting that those mid-gap states do not play a role in the up-conversion mechanism except as a loss pathway.

Chapter 4 demonstrates the optical cooling of CsPbBr₃ nanocrystals via efficient ASPL. I show that the spectral shape and position of CsPbBr₃ ASPL changes during below gap excitation in a manner that is consistent with the nanoparticles getting colder. Additionally, I show that the ASPL yield exponentially decreases over time. This change in ASPL yield is reversible when the nanocrystals are left in the dark, or if the excitation fluence is decreased. As ASPL is a thermally activated process, a reversible decrease in ASPL yield is consistent with the nanoparticles getting colder during below-gap excitation. The relationship between temperature and ASPL yield is known to follow an Arrhenius, and so I show how the change in ASPL yield can be used to estimate the change in nanoparticle temperature. Further, I use a Raman thermometric technique to demonstrate that the CsPbBr₃ nanoparticles are cooling their local environment—in this case, a silicon substrate—by up to 25 degrees.

Chapter 5 shows how coupling CsPbBr₃ nanocrystals to a plasmonic substrate can enhance the thermal scavenging potential of the CsPbBr₃ ASPL. The ASPL intensity as well as the magnitude of the anti-Stokes shift between the absorbed and emitted photons are key to determining the amount of thermal energy that can be removed by ASPL per unit time. I show that CsPbBr₃ ASPL blue shifts when coupled to gold nanoparticles. Further, when coupled to a monolayer film of gold nanoparticles, the ASPL both blue shifts and increases in intensity relative to the CsPbBr₃ SSPL. The combination of these two effects is determined to increase the ASPL thermal scavenging potential 6.7-fold over CsPbBr₃ alone.

CsPbBr₃ nanocrystals provide a unique opportunity to study optical processes at their thermodynamic limit. This is especially typified by their successful cooling via ASPL, a phenomenon that requires near lossless emission efficiency. Still, much is unknown or not well understood about their ASPL and the limits of its practical application. While I have established that the defect states associated with excess lead on the CsPbBr₃ surfaces is unlikely to act as an intermediate state for ASPL, whether or not there is an intermediate state has yet to be determined. Additionally, the anti-Stokes shifts observed require more thermal energy than seems statistically likely given the number of longitudinal optical phonons required, as has already received some commentary in the literature. [53] These fundamental mechanistic questions require further study if CsPbBr₃ ASPL is to be optimized for application in macroscopic cooling devices.

REFERENCES

- [1] L. Protesescu, S. Yakunin, M. I. Bodnarchuk, F. Krieg, R. Caputo, C. H. Hendon, R. X. Yang, A. Walsh, M. V. Kovalenko. *Nano Lett* **2015**, *15*, 3692-3696.
- [2] G. Li, H. Wang, T. Zhang, L. Mi, Y. Zhang, Z. Zhang, W. Zhang, Y. Jiang. *Adv Funct Mater* **2016**, *26*, 8478-8486.
- [3] X. Zhang, B. Xu, J. Zhang, Y. Gao, Y. Zheng, K. Wang, X. W. Sun. *Adv Funct Mater* **2016**, *26*, 4595-4600.
- [4] F. Chen, K. M. Boopathi, M. Imran, S. Lauciello, M. Salerno. *Materials (Basel)* **2020**, *13*,
- [5] Q. Zhang, R. Su, X. Liu, J. Xing, T. C. Sum, Q. Xiong. *Adv Funct Mater* **2016**, *26*, 6238-6245.
- [6] Y. Fu, H. Zhu, C. C. Stoumpos, Q. Ding, J. Wang, M. G. Kanatzidis, X. Zhu, S. Jin. *ACS Nano* **2016**, *10*, 7963-7972.
- [7] T. Masuda, Y. Zhang, C. Ding, F. Liu, K. Sasaki, Q. Shen, M. Endo. *J Appl Phys* **2020**, *127*, 243104.
- [8] J. Liang, C. Wang, Y. Wang, Z. Xu, Z. Lu, Y. Ma, H. Zhu, Y. Hu, C. Xiao, X. Yi, G. Zhu, H. Lv, L. Ma, T. Chen, Z. Tie, Z. Jin, J. Liu. *J Am Chem Soc* **2016**, *138*, 15829-15832.
- [9] C. Liu, W. Li, C. Zhang, Y. Ma, J. Fan, Y. Mai. *J Am Chem Soc* **2018**, *140*, 3825-3828.

- [10] K. Wang, Z. Jin, L. Liang, H. Bian, D. Bai, H. Wang, J. Zhang, Q. Wang, S. Liu. *Nat Commun* **2018**, *9*, 4544.
- [11] C. Guhrenz, A. Benad, C. Ziegler, D. Haubold, N. Gaponik, A. Eychmüller. *Chem Mater* **2016**, *28*, 9033-9040.
- [12] G. Nedelcu, L. Protesescu, S. Yakunin, M. I. Bodnarchuk, M. J. Grotevent, M. V. Kovalenko. *Nano Lett* **2015**, *15*, 5635-5640.
- [13] S. E. Creutz, E. N. Crites, M. C. De Siena, D. R. Gamelin. *Chem Mater* **2018**, *30*, 4887-4891.
- [14] D. Zhang, Y. Yang, Y. Bekenstein, Y. Yu, N. A. Gibson, A. B. Wong, S. W. Eaton, N. Kornienko, Q. Kong, M. Lai, A. P. Alivisatos, S. R. Leone, P. Yang. *J Am Chem Soc* **2016**, *138*, 7236-7239.
- [15] J. De Roo, M. Ibáñez, P. Geiregat, G. Nedelcu, W. Walravens, J. Maes, J. C. Martins, I. Van Driessche, M. V. Kovalenko, Z. Hens. *ACS Nano* **2016**, *10*, 2071-2081.
- [16] D. P. Nenon, K. Pressler, J. Kang, B. A. Koscher, J. H. Olshansky, W. T. Osowiecki, M. A. Koc, L. W. Wang, A. P. Alivisatos. *J Am Chem Soc* **2018**, *140*, 17760-17772.
- [17] L. M. Wheeler, E. M. Sanehira, A. R. Marshall, P. Schulz, M. Suri, N. C. Anderson, J. A. Christians, D. Nordlund, D. Sokaras, T. Kroll, S. P. Harvey, J. J. Berry, L. Y. Lin, J. M. Luther. *J Am Chem Soc* **2018**, *140*, 10504-10513.
- [18] G. E. Eperon, D. S. Ginger. *ACS Energy Lett* **2017**, *2*, 1190-1196.

- [19] J. Kang, L. W. Wang. *J Phys Chem Lett* **2017**, *8*, 489-493.
- [20] S. ten Brinck, F. Zaccaria, I. Infante. *ACS Energy Lett* **2019**, *4*, 2739-2747.
- [21] B. A. Koscher, J. K. Swabeck, N. D. Bronstein, A. P. Alivisatos. *J Am Chem Soc* **2017**, *139*, 6566-6569.
- [22] B. A. Koscher, Z. Nett, A. P. Alivisatos. *ACS Nano* **2019**, *13*, 11825-11833.
- [23] H. Dong, L. D. Sun, C. H. Yan. *Chem Soc Rev* **2015**, *44*, 1608-1634.
- [24] C. Duan, L. Liang, L. Li, R. Zhang, Z. P. Xu. *J Mater Chem B* **2018**, *6*, 192-209.
- [25] Y. Shang, S. Hao, C. Yang, G. Chen. *Nanomaterials (Basel)* **2015**, *5*, 1782-1809.
- [26] S. Asahi, H. Teranishi, K. Kusaki, T. Kaizu, T. Kita. *Nat Commun* **2017**, *8*, 14962.
- [27] X. Zhu, J. Zhang, J. Liu, Y. Zhang. *Adv Sci (Weinh)* **2019**, *6*, 1901358.
- [28] G. Chen, J. Damasco, H. Qiu, W. Shao, T. Y. Ohulchanskyy, R. R. Valiev, X. Wu, G. Han, Y. Wang, C. Yang, H. Ågren, P. N. Prasad. *Nano Lett* **2015**, *15*, 7400-7407.
- [29] A. E. Ragab, A.-S. Gadallah, M. B. Mohamed, I. M. Azzouz. *Opt Laser Technol* **2014**, *63*, 8-12.
- [30] A. G. Joly, W. Chen, D. E. McCready, J.-O. Malm, J.-O. Bovin. *Phys Rev B* **2005**, *71*,
- [31] J. Ouyang, J. A. Ripmeester, X. Wu, D. Kingston, K. Yu, A. G. Joly, W. Chen. *J Phys Chem C* **2007**, *111*, 16261-16266.
- [32] Z. Deutsch, L. Neeman, D. Oron. *Nat Nanotechnol* **2013**, *8*, 649-653.

- [33] A. H. Khan, G. H. V. Bertrand, A. Teitelboim, C. Sekhar M, A. Polovitsyn, R. Brescia, J. Planelles, J. I. Climente, D. Oron, I. Moreels. *ACS Nano* **2020**, *14*, 4206-4215.
- [34] Y. Dong, J. Choi, H. K. Jeong, D. H. Son. *J Am Chem Soc* **2015**, *137*, 5549-5554.
- [35] G. V. Naik, J. A. Dionne. *Appl Phys Lett* **2015**, *107*, 133902.
- [36] G. V. Naik, A. J. Welch, J. A. Briggs, M. L. Solomon, J. A. Dionne. *Nano Lett* **2017**, *17*, 4583-4587.
- [37] A. E. Saunders, I. Popov, U. Banin. *J Phys Chem B* **2006**, *110*, 25421-25429.
- [38] S. K. Dutta, S. K. Mehetor, N. Pradhan. *J Phys Chem Lett* **2015**, *6*, 936-944.
- [39] K. Wu, W. E. Rodríguez-Córdoba, Y. Yang, T. Lian. *Nano Lett* **2013**, *13*, 5255-5263.
- [40] A. Demortière, R. D. Schaller, T. Li, S. Chattopadhyay, G. Krylova, T. Shibata, P. C. dos Santos Claro, C. E. Rowland, J. T. Miller, R. Cook, B. Lee, E. V. Shevchenko. *J Am Chem Soc* **2014**, *136*, 2342-2350.
- [41] E. Khon, A. Mereshchenko, A. N. Tarnovsky, K. Acharya, A. Klinkova, N. N. Hewa-Kasakarage, I. Nemitz, M. Zamkov. *Nano Lett* **2011**, *11*, 1792-1799.
- [42] S. K. Balakrishnan, P. V. Kamat. *ACS Energy Lett* **2017**, *2*, 88-93.
- [43] B. J. Roman, J. Otto, C. Galik, R. Downing, M. Sheldon. *Nano letters* **2017**, *17*, 5561-5566.
- [44] F. A. Rodríguez Ortiz, B. J. Roman, J. R. Wen, N. Mireles Villegas, D. F. Dacres, M. T. Sheldon. *Nanoscale* **2019**, *11*, 18109-18115.

- [45] M. Sheik-Bahae, R. I. Epstein. *Phys Rev Lett* **2004**, *92*, 247403.
- [46] D. V. Seletskiy, R. Epstein, M. Sheik-Bahae. *Rep Prog Phys* **2016**, *79*, 096401.
- [47] M. Sheik-Bahae, R. I. Epstein. *Nat Photonics* **2007**, *1*, 693-699.
- [48] Y. P. Rakovich, J. F. Donegan, M. I. Vasilevskiy, A. L. Rogach. *physica status solidi (a)* **2009**, *206*, 2497-2509.
- [49] S.-T. Ha, C. Shen, J. Zhang, Q. Xiong. *Nat Photonics* **2016**, *10*, 115-121.
- [50] J. Zhang, D. Li, R. Chen, Q. Xiong. *Nature* **2013**, *493*, 504-508.
- [51] S. D. Melgaard, A. R. Albrecht, M. P. Hehlen, M. Sheik-Bahae. *Sci Rep* **2016**, *6*, 20380.
- [52] J. B. Khurgin. *Phys Rev B* **2008**, *77*,
- [53] A. Granados del Águila, T. T. H. Do, J. Xing, W. J. Jee, J. B. Khurgin, Q. Xiong. *Nano Res* **2020**, *13*, 1962-1969.
- [54] S. Ye, M. Zhao, M. Yu, M. Zhu, W. Yan, J. Song, J. Qu. *J Phys Chem C* **2018**, *122*, 3152-3156.
- [55] S. Zhang, M. Zhukovskyi, B. Jankó, M. Kuno. *NPG Asia Mater* **2019**, *11*, 1-19.
- [56] Y. V. Morozov, S. Draguta, S. Zhang, A. Cadranet, Y. Wang, B. Janko, M. Kuno. *J Phys Chem C* **2017**, *121*, 16607-16616.
- [57] B. J. Roman, M. Sheldon. *Chem Commun* **2018**, *54*, 6851-6854.
- [58] X. Ma, F. Pan, H. Li, P. Shen, C. Ma, L. Zhang, H. Niu, Y. Zhu, S. Xu, H. Ye. *J Phys Chem Lett* **2019**, *10*, 5989-5996.

- [59] I. Schnitzer, E. Yablonovitch, C. Caneau, T. J. Gmitter. *Appl Phys Lett* **1993**, *62*, 131-133.
- [60] Y. V. Morozov, S. Zhang, A. Pant, B. Jankó, S. D. Melgaard, D. A. Bender, P. J. Pauzauskie, M. Kuno. *Nature* **2019**, *570*, E60-E61.
- [61] W. van der Stam, J. J. Geuchies, T. Altantzis, K. H. W. van den Bos, J. D. Meeldijk, S. Van Aert, S. Bals, D. Vanmaekelbergh, C. de Mello Donega. *J Am Chem Soc* **2017**, *139*, 4087-4097.
- [62] G. Menagen, D. Mocatta, A. Salant, I. Popov, D. Dorfs, U. Banin. *Chem Mater* **2008**, *20*, 6900-6902.
- [63] S. E. Habas, P. Yang, T. Mokari. *J Am Chem Soc* **2008**, *130*, 3294-3295.
- [64] T. Mokari, E. Rothenberg, I. Popov, R. Costi, U. Banin. *Science* **2004**, *304*, 1787-1790.
- [65] M. T. Sheldon, P. E. Trudeau, T. Mokari, L. W. Wang, A. P. Alivisatos. *Nano Lett* **2009**, *9*, 3676-3682.
- [66] Y. Ben-Shahar, F. Scotognella, I. Kriegel, L. Moretti, G. Cerullo, E. Rabani, U. Banin. *Nat Commun* **2016**, *7*,
- [67] E. Shaviv, O. Schubert, M. Alves-Santos, G. Goldoni, R. Di Felice, F. Vallée, N. Del Fatti, U. Banin, C. Sönnichsen. *ACS Nano* **2011**, *5*, 4712-4719.
- [68] N. Matsushita, F. Fukuhara, N. Kojima. *Acta Crystallographica Section E Structure Reports Online* **2005**, *61*, i123-i125.

- [69] X. J. Liu, K. Matsuda, Y. Moritomo, A. Nakamura, N. Kojima. *Phys Rev B* **1999**, *59*, 7925.
- [70] M. Lorenzon, L. Sortino, Q. Akkerman, S. Accornero, J. Pedrini, M. Prato, V. Pinchetti, F. Meinardi, L. Manna, S. Brovelli. *Nano Lett* **2017**, *17*, 3844-3853.
- [71] P. Cottingham, R. L. Brutchey. *Chem Commun (Camb)* **2016**, *52*, 5246-5249.
- [72] L. J. Chen, C. R. Lee, Y. J. Chuang, Z. H. Wu, C. Chen. *J Phys Chem Lett* **2016**, *7*, 5028-5035.
- [73] T. C. Jellicoe, J. M. Richter, H. F. Glass, M. Tabachnyk, R. Brady, S. E. Dutton, A. Rao, R. H. Friend, D. Credginton, N. C. Greenham, M. L. Böhm. *J Am Chem Soc* **2016**, *138*, 2941-2944.
- [74] B.-W. Park, B. Philippe, X. Zhang, H. Rensmo, G. Boschloo, E. M. J. Johansson. *Adv Mater* **2015**, *27*, 6806-6813.
- [75] B. Saparov, F. Hong, J.-P. Sun, H.-S. Duan, W. Meng, S. Cameron, I. G. Hill, Y. Yan, D. B. Mitzi. *Chem Mater* **2015**, *27*, 5622-5632.
- [76] X. Wu, G. Chen, J. Shen, Z. Li, Y. Zhang, G. Han. *Bioconjug Chem* **2015**, *26*, 166-175.
- [77] X. Huang, S. Han, W. Huang, X. Liu. *Chem Soc Rev* **2013**, *42*, 173-201.
- [78] T. N. Singh-Rachford, F. N. Castellano. *Coord Chem Rev* **2010**, *254*, 2560-2573.
- [79] X. Wang, W. W. Yu, J. Zhang, J. Aldana, X. Peng, M. Xiao. *Phys Rev B* **2003**, *68*,
- [80] Y. P. Rakovich, S. A. Filonovich, M. J. M. Gomes, J. F. Donegan, D. V. Talapin, A. L. Rogach, A. Eychmüller. *physica status solidi (b)* **2002**, *229*, 449-452.

- [81] I. V. Ignatiev, I. E. Kozin, H.-W. Ren, S. Sugou, Y. Masumoto. *Phys Rev B* **1999**, *60*, R14001.
- [82] E. Poles, D. C. Selmarten, O. I. Mičić, A. J. Nozik. *Appl Phys Lett* **1999**, *75*, 971-973.
- [83] N. Akizuki, S. Aota, S. Mouri, K. Matsuda, Y. Miyauchi. *Nat Commun* **2015**, *6*, 8920.
- [84] Y. V. Morozov, S. Zhang, M. C. Brennan, B. Janko, M. Kuno. *ACS Energy Lett* **2017**, *2*, 2514-2515.
- [85] C. M. Iaru, J. J. Geuchies, P. M. Koenraad, D. Vanmaekelbergh, A. Y. Silov. *ACS Nano* **2017**, *11*, 11024-11030.
- [86] J. Mooney, M. M. Krause, J. I. Saari, P. Kambhampati. *Phys Rev B* **2013**, *87*,
- [87] P. Pringsheim. *Zeitschrift für Physik* **1929**, *57*, 739-746.
- [88] J. L. Clark, G. Rumbles. *Phys Rev Lett* **1996**, *76*, 2037.
- [89] J. L. Clark, P. F. Miller, G. Rumbles. *J Phys Chem A* **1998**, *102*, 4428-4437.
- [90] O. Dimitriev, A. Fedoryak, Y. Slominskii, A. Smirnova, T. Yoshida. *Chem Phys Lett* **2020**, *738*, 136905.
- [91] G. Rupper, N. H. Kwong, R. Binder. *physica status solidi (c)* **2006**, *3*, 2489-2493.
- [92] D. A. Bender, J. G. Cederberg, C. Wang, M. Sheik-Bahae. *Appl Phys Lett* **2013**, *102*, 252102.
- [93] C. Wang, C.-Y. Li, M. P. Hasselbeck, B. Imangholi, M. Sheik-Bahae. *J Appl Phys* **2011**, *109*, 093108.

- [94] D. A. Hanifi, N. D. Bronstein, B. A. Koscher, Z. Nett, J. K. Swabeck, K. Takano, A. M. Schwartzberg, L. Maserati, K. Vandewal, Y. van de Burgt, A. Salleo, A. P. Alivisatos. *Science* **2019**, *363*, 1199-1202.
- [95] B. J. Roman, M. T. Sheldon. *Nanophotonics* **2019**, *8*, 599-605.
- [96] C. Würth, M. Grabolle, J. Pauli, M. Spieles, U. Resch-Genger. *Nat Protoc* **2013**, *8*, 1535-1550.
- [97] G. Rainò, A. Landuyt, F. Krieg, C. Bernasconi, S. T. Ochsenein, D. N. Dirin, M. I. Bodnarchuk, M. V. Kovalenko. *Nano Lett* **2019**, *19*, 3648-3653.
- [98] F. Herrmann, P. Würfel. *Am J Phys* **2005**, *73*, 717-721.
- [99] R. Bhattacharya, B. Pal, B. Bansal. *Appl Phys Lett* **2012**, *100*, 222103.
- [100] R. Saran, A. Heuer-Jungemann, A. G. Kanaras, R. J. Curry. *Adv Opt Mater* **2017**, *5*, 1700231.
- [101] M. Cardona. **1982**, *Light Scattering in Solids II*, 19-178.
- [102] Y. S. Yamamoto, Y. Ozaki, T. Itoh. *J Photochem and Photobiol C* **2014**, *21*, 81-104.
- [103] P. B. Johnson, R.-W. J. P. Christy. *Phys Rev B* **1972**, *6*, 4370.
- [104] D. N. Dirin, I. Cherniukh, S. Yakunin, Y. Shynkarenko, M. V. Kovalenko. *Chem Mater* **2016**, *28*, 8470-8474.
- [105] T. Hartsfield, M. Gegg, P.-H. Su, M. R. Buck, J. A. Hollingsworth, C.-K. Shih, M. Richter, H. Htoon, X. Li. *ACS Photonics* **2016**, *3*, 1085-1089.
- [106] G. Sun, R. Chen, Y. J. Ding, J. B. Khurgin. *ACS Photonics* **2015**, *2*, 628-632.

[107]D. Kim, H. Yokota, T. Taniguchi, M. Nakayama. *J of Appl Phys* **2013**, *114*, 154307.